PROCESSING HIGH PURITY ZIRCONIUM DIBORIDE ULTRA-HIGH TEMPERATURE CERAMICS: SMALL-TO-LARGE SCALE PROCESSING

by

David Pham

A Dissertation Submitted to the Faculty of the

DEPARTMENT OF MATERIALS SCIENCE AND ENGINEERING

In Partial Fulfillment of the Requirements
For the Degree of

DOCTOR OF PHILOSOPHY

In the Graduate College

THE UNIVERSITY OF ARIZONA

2016

THE UNIVERSITY OF ARIZONA
GRADUATE COLLEGE

As members of the Dissertation Committee, we certify that we have read the dissertation prepared by David Pham, titled Processing High Purity Zirconium Diboride Ultra-High Temperature Ceramics: Small-to-Large Scale Processing and recommend that it be accepted as fulfilling the dissertation requirement for the Degree of Doctor of Philosophy.

_____ Date: 12/3/2015
Erica L. Corral

_____ Date: 12/3/2015
Krishna Muralidharan

_____ Date: 12/3/2015
Doug Loy

_____ Date: 12/3/2015
Venkateswara R. Manga

Final approval and acceptance of this dissertation is contingent upon the candidate's submission of the final copies of the dissertation to the Graduate College.

I hereby certify that I have read this dissertation prepared under my direction and recommend that it be accepted as fulfilling the dissertation requirement.

_____ Date: 12/3/2015

Dissertation Director: Erica L. Corral

STATEMENT BY AUTHOR

This dissertation has been submitted in partial fulfillment of the requirements for an advanced degree at the University of Arizona and is deposited in the University Library to be made available to borrowers under rules of the Library.

SIGNED: David Pham

ACKNOWLEDGEMENTS

Professional Acknowledgements

First, I'd like to thank all of the collaborators who have supplied their expertise to develop the following body of work. I'd like to thank Dr. Krishna Muralidharan and Dr. Venkateswara R. Manga from the University of Arizona, Materials Science and Engineering Department for helping develop the thermodynamic models. Without their expertise in CALPHAD based modeling, the phase equilibria diagrams could not have been made to allow microstructure predictions. I'd also like to thank Dr. James LeBeau and Joseph Houston Dycus from North Carolina State University in aiding us with the microstructural characterization of our ceramics using scanning electron transmission microscopy. The knowledge they have provided has allowed us to develop a better understanding in the processing of ultra-high temperature ceramics.

Personal Acknowledgements

I would like to thank my advisor, Dr. Erica Corral for her patience and guidance while pursuing my degree. Dr. Corral was highly influential in my decision to pursue my doctorates at the UofA. Even when Murphy's law would sneak its way into the lab, we were able to reach our goals and come out on top.

I would like to send out my appreciation to all the professors at the UofA whom I've had the pleasure of taking a class with. Their enthusiasm for teaching and knack for making classes I had no familiarity with interesting made for a great learning experience.

I'd also like to thank my advisor at the University of Texas at El Paso, Dr. Arturo Bronson for his guidance and showing me the road into Materials Science and Engineering. He is one mentor whom I have not given enough thanks to over the years, and so I dedicate this section to him.

Finally, I'd like to send my deepest thanks and appreciation to all my family and friends for their loving support and understanding. You've been there during my trials and tribulations - allowing me to selfishly vent out my frustrations: (ノ°□°)ノ ┻━┻ and geek out to the max: d=(´▽｀)=b.

Table of Contents

List of Figures

List of Tables

Abstract

Next generation aerospace vehicles require thermal protection system (TPS) materials that are capable of withstanding the extreme aerothermal environment during hypersonic flight (>Mach 5 [>1700 m/s]). Ultra-high temperature ceramics (UHTC) such as zirconium diboride (ZrB_2) are candidate TPS materials due to their high-temperature thermal and mechanical properties and are often the basis for advanced composites for enhanced oxidation resistance. However, ZrB_2 matrix impurities in the form of boron trioxide (B_2O_3) and zirconium dioxide (ZrO_2) limit the high-temperature capabilities. Electric based sintering techniques, such as spark plasma sintering (SPS), that use joule heating have become the preferred densification method to process advanced ceramics due to its ability to produce high density parts with reduced densification times and limit grain growth. This study focuses on a combined experimental and thermodynamic assisted processing approach to enhance powder purity through a carbo- and borocarbo-thermal reduction of oxides using carbon (C) and boron carbide (B_4C). The amount of oxides on the powder surface are measured, the amount of additive required to remove oxides is calculated, and processing conditions (temperature, pressure, environment) are controlled to promote favorable thermodynamic reactions both during thermal processing in a tube furnace and SPS. Untreated ZrB_2 contains 0.18 wt%O after SPS. Additions of 0.75 wt%C is found to reduce powder surface oxides to 0.12 wt%O. A preliminary Zr-C-O computational thermodynamic model shows limited efficiency of carbon additions to completely remove oxygen due to the solubility of oxygen in zirconium carbide (ZrC) forming a zirconium oxycarbide (ZrC_xO_y). Scanning electron microscopy (SEM) and scanning transmission electron microscopy (STEM) with atomic scale elemental

spectroscopy shows reduced oxygen content with amorphous Zr-B oxides and discreet ZrO_2 particle impurities in the microstructure. Processing ZrB_2 with minimal additions of B_4C (0.25 wt%) produces high purity parts after SPS with only 0.06 wt%O. STEM identifies unique "trash collector" oxides composed of manufacturer powder impurities of calcium, silver, and yttrium. A preliminary Zr-B-C-O thermodynamic model is used to show the potential reaction paths using B_4C that promotes oxide removal to produce high-purity ZrB_2 with fine grains (3.3 μm) and superior mechanical properties (flexural strength of 660MPa) than the current state-of-the-art ZrB_2 ceramics. Due to the desirable properties produced using SPS, there is growing interest to advance processing techniques from lab-scale (20 mm discs) to large-scale (>100 mm). The advancement of SPS technologies has been stunted due to the limited power and load delivery of lab-scale furnaces. We use a large scale direct current sintering furnace (DCS) to address the challenges of producing industrially relevant sized parts. However, current-assisted sintering techniques, like SPS and DCS, are highly dependent on tooling resistances and the electrical conductivity of the sample, which influences the part uniformity through localized heating spots that are strongly dependent on the current flow path. We develop a coupled thermal-electrical finite element analysis model to investigate the development and effects of tooling and current density manipulation on an electrical conductor (ZrB_2) and an electrical insulator, silicon nitride (Si_3N_4), at the steady-state where material properties, temperature gradients and current/voltage input are constant. The model is built based on experimentally measured temperature gradients in the tooling for 20 mm discs and validated by producing 30 mm discs with similar temperature gradients and grain size uniformity across the part.

The model aids in developing tooling to manipulate localize current density in specific regions to produce uniform 100 mm discs of ZrB_2 and Si_3N_4.

CHAPTER 1

Executive Summary

1.1 Spark Plasma Sintering Of Zirconium Diboride Using Carbon as an Oxide Reducing Agent. Part 1: Densification Behavior and Microstructural Analysis

This study shows novelty in the investigation of microstructural and grain boundary impurities found in ZrB_2 processed with carbon as an oxide reducing agent and spark plasma sintering (SPS). Carbon is commonly used to reduce oxygen impurities found on the ZrB_2 powder surface, however, there is little understanding in how the microstructures evolve based on the oxygen content found in the powder prior to sintering by SPS. The following are key findings in this study:

1. ZrB_2 is processed with specific carbon additions to target a measured ZrO_2 on the powder surface.
2. Scanning transmission electron microscopy with high resolution elemental mapping is used to identify the grain boundary chemistry. Grain boundaries contain low melting metal impurities from milling and manufacturer impurities of cobalt and iron.
3. By using carbon, additional microstructural impurities of discreet ZrO_2 particles are identified. These impurities are distributed throughout the microstructure by standard oxide impurities and in thin layers in the grain boundaries.

4. It is not recommended to use carbon as an oxide reducing agent due to the formation of discreet oxide impurities and insignificant reduction in grain size and total oxygen content measure after SPS.

1.2 Spark Plasma Sintering Of Zirconium Diboride Using Carbon as an Oxide Reducing Agent. Part 2: Thermodynamic Analysis of Impurity Phases

A thermodynamic model of the Zr-C-O system is developed in order to understand the development of microstructural impurities during the processing of ZrB_2 with carbon. Through the work in this investigation, the following is established:

1. We developed a thermodynamic model that can be used to identify the phase equilibria in the Zr-C-O system.
2. The model can be used as a predictive tool for microstructures found through the analysis of the ZrO_2-C and Zr-C-O phase diagrams.
3. The phase diagrams show how microstructures retain oxygen through the formation of zirconium oxycarbides that are predicted to precipitate into ZrO_2 particle impurities.
4. By applying the same methodology, a foundation is made to allow the model to advance into similar metal diboride systems of titanium and hafnium, allowing for extensive thermodynamic analysis to be performed prior to processing and densification to identify the most effective processing methods for low oxygen content UHTCs.

1.3 SPS Densification of Zirconium Diboride With Boron Carbide Additions

A thermodynamic model of the Zr-B-C-O system is developed in order to understand the effectiveness of boron carbide to remove ZrB_2 surface oxides.. The novelty of this work is highlighted in the following:

1. We develop the first thermodynamic model of the Zr-B-C-O system.
2. The model is used to identify the phase equilibria involved with the removal of ZrB_2 surface oxides and boron carbide.
3. The pseudo binary ZrO_2-B_4C and psuedo-ternary phase diagrams of the ZrB_2-ZrO_2-B_4C phase diagrams show effective removal of surface oxides to form ZrB_2 or volatile oxide species.
4. ZrB_2 processed with B_4C produces a low oxygen content ceramic with fine grain sizes and superior room temperature strength.
5. This study shows the potential for the Zr-B-C-O thermodynamic model to be used a predictive tool for advanced material processing.
6. The Zr-B-C-O model can be advanced to include additional compounds to predict microstructures for UHTC composites.

1.4 Scale Up Processing Using Finite Element Analysis Modeling of SPS

We have produced ZrB_2 with superior mechanical properties and low oxygen impurity content after processing with B_4C and SPS in small lab-scale 20mm disc samples in the previous studies. In this study we focus on producing a predictive model and find the following:

1. We produced a finite element analysis based model, with coupled heat transfer and joule heating physics, to predict sample temperature gradients that are present during spark plasma sintering of both ZrB_2, an electrical conductor, and Si_3N_4, an electrical insulator.
2. We show how the model should be developed by considering all the relevant thermal and electrical boundary conditions in SPS.
3. Experimental results are modeled to obtain a model to scale a 20mm disc to a 30mm disc with identical microstructural properties.
4. Experimental results with Si_3N_4 shows a need to evolve the model with an additional mechanical coupling to predict mechanical loading for materials with phase transition sensitivity to stresses.
5. The model shows potential as a predictive engineering tool for temperature gradients along a sintered part. Tooling is proposed to produce 100mm discs with uniform sample temperature gradients equivalent to a 20mm disc.
6. Comparing the model to literature, it is suggested that each model should be calibrated based on the individual SPS manufacturer and material properties to predict sample temperature gradients.

CHAPTER 2

Background and Introduction

2.1 Hypersonic Flight

Hypersonic flight encompasses systems with velocities greater than Mach 5 (1,700 m/s), 5 times greater than the speed of sound. These systems include high-speed interceptor missiles, space access vehicles, hypersonic cruise aircraft, and re-entry vehicles, which have increasing speed demands for fast-response defense applications and rapid global transportation. When hypersonic vehicles slice through the air, they generate high energy shock waves that increases the surrounding air temperature and modifies the atmosphere into dissociated air. Thus, the leading edges are exposed to extreme thermal and mechanical stress in a highly reactive environment. Further, to enhance vehicle maneuverability and enhance flight safety, the leading edges require sharp profiles, which compounds the environmental stresses a leading edge must withstand and adds the requirement of a non-changing shape profile[1].

Traditional materials include fibrous refractory composite insulations tiles, as found on space shuttles, fused-silica or silicon nitride for missile radomes, and ablative graphite composites for re-entry vehicles. In order to reduce the price for space access vehicles, material systems for re-entry vehicles must be reusable. Thus, next generation aerospace vehicles require thermal protection system (TPS) materials that can withstand the mechanical and chemical environment of hypersonic flight[2].

2.2 Ultra-High Temperature Ceramics (UHTCS)

Ultra-high temperature materials are a classification of materials that are candidates for hypersonic TPS with melting points above 2400°C, with the exception of silicon carbide (SiC) and carbon that do not melt in ambient pressure. These materials are limited to a handful of pure metals, oxides, borides, carbides, and nitrides. Pure metals, like tungsten and rhenium, will readily oxidize, and non-oxides of niobium and titanium will oxidize rapidly in the hypersonic environment, forming oxides with low melting temperatures (<1900°C)[3]. Oxides have low thermal conductivity, which prevents heat dissipation on the leading edge and have lower strengths than non-oxides. Carbon is resistant to high temperatures, but ablates rapidly through the formation of CO_2 and CO gases. Therefore, the available material systems that have potential for reusable hypersonic vehicles is very limited.

Of particular interest for the hypersonic leading edge, are SiC and the transition metal borides and carbides of zirconium (ZrB_2, ZrC) and hafnium (HfB_2, HfC), which are referred to as ultra-high temperature ceramics (UHTCs). These UHTCs all oxidize in the hypersonic environment, however, as composites, they become more resistant to oxidation with enhanced mechanical properties. While ZrC and HfC oxidize forming non-protective and porous ZrO_2 and HfO_2 scales, they also exhibit the highest melting temperatures. The diborides form ZrO_2 and a B_2O_3 oxide scales that are protective up to 1200°C. SiC forms an SiO_2 oxide that is protective up to 1500°C, but actively oxidizes in low oxygen pressures forming SiO gas. ZrB_2 and HfB_2 are used as the matrix material for UHTC composites due to the high thermal and electrical conductivity. ZrC can be added to improve mechanical strength of the composite and SiC is added to enhance the oxidation resistance.

ZrB_2+SiC composites oxidize to form a $ZrO_2 \cdot SiO_2 \cdot B_2O_3$ glass scale with enhanced oxidation resistance.

2.3 Crystal Structure and Property Relations

ZrB_2 and HfB_2 are very similar and share the same hexagonal crystal structure (P6/mmm space group). The crystal structure contains hexagonally close-packed metal atoms (Me) that alternate with boron (B) atoms in a graphite-like network. The combination of Me-Me, Me-B, and B-B bonds provide the characteristic properties of diborides. Me-Me bonds contribute to the intrinsically high thermal and electrical conductivities, Me-B bonds have ionic bonding characteristics that influence the thermal stability of the diboride while the B-B bond strength is responsible for the refractory characteristics of diborides, providing higher melting temperatures, hardness, and strength[4]. As such, processing diborides requires very high temperatures and are consolidated using powder processing techniques.

2.4 Powder Processing

UHTC composites can strengthen specific desired properties as discussed in Section 1.2. However, UHTC composites are limited in their high-temperature capabilities due to the impurities found in the matrix material. Ceramic powder processing involves the communition or de-agglomeration of powder particles and further size reduction. This can be done through various communition techniques like attrition milling, hammer milling, ball milling, and ultrasonic mixing. As a result, the powder surface area increases and becomes subject to oxidation in ambient. These oxide impurities are then present throughout the microstructure and encourage coarsening, or grain growth, mechanisms during densification. Coarsening mechanisms arise from vapor and surface diffusion

which allows material to rearrange and move without particle centers coming together. Grain boundary diffusion, which allows material from the particle center to neck, or join, with a neighboring particle and move outwards to fill porosity, is inhibited.

In order to reduce surface oxide impurities while maintaining high surface areas, there has been a push in the development of sol-gel processing techniques for UHTCs. Sol-gel processing is a liquid chemical based technique that uses controlled nucleation and growth of colloidal particles. Sol-gel processing has produced high purity UHTCs, however, they are sensitive to batch sizes and difficult to produce in mass. Although various sol-gel recipes for ZrB_2 are published[5–8], densification of sol-gel derived powders is scarce[9] and currently no thermo-mechanical characterization of bulk sample exist.

The alternative and more affordable approach is to enhance powder purity by applying a thermodynamic reduction of oxides. Carbon, boron carbide, boron and other carbides that react with oxygen to form solid solution byproducts with ZrB_2 have been applied. The use of oxide reducing agents has shown to enhance sinterability of ZrB_2 and improve mechanical properties. The use of reducing additives is typically used in excess to attempt to remove the most oxides possible which generates additional impurity phases in the microstructure. This dissertation focuses on applying a thermodynamic approach with a calculated approach to remove oxides.

2.5 Densification of UHTCs

There is constant evolution in methods for the densification or consolidation of ceramic powders. In general, densification methods can be split into two categories: 1) traditional radiative heating methods and 2) novel electrically-assisted techniques.

2.5.1 Pressureless Sintering and Hot Pressing

The two most commonly used techniques that use radiative heating are pressureless sintering and hot pressing. Pressureless sintering utilizes a pre-shaped powder compact and placed in a furnace where temperatures are increased with limited sample heating rates (an average of 20°C/min). These furnaces include tube furnaces and box furnaces with $MoSi_2$ or graphite resistive heating elements. The sole driving force for pressureless sintering is the reduction of particle surface area. Presureless sintering is a highly attractive method for densification due to the ability to produce parts with complex geometries that can minimize post-processing costs. However, UHTCs have extreme difficulty consolidating to high density (>95% theoretical density) without the use of sintering aids, extreme temperatures (2100°C), and long hold times (>1hr).

Hot pressing contains the powder compact in a vessel and a uniaxial load is applied during heating. The vessel is typically made of heat resistant materials such as graphite; other materials such as SiC and WC have also been used where applied loads are greater than 100MPa. By applying a load on the contained powder compact, interparticle stresses and particle contact surfaces increase to amplify the driving force for sintering. Further, at high temperatures, creep mechanisms encourage material flow to fill pores and obtain high density parts. Hot pressing decreases the time and temperature for sintering, which encourages the production of finer grained parts with higher mechanical properties. Hot pressing can produce complex shapes with an emphasis on engineering tooling.

2.5.2 Spark Plasma Sintering

Electrically-assisted sintering techniques are various - the focus of this dissertation will be on spark plasma sintering (SPS). Briefly, other techniques include microwave

sintering, FLASH sintering which uses high voltage, and induction heating and sintering. SPS is becoming the preferred method of densification due to the ability to produce novel materials through the simultaneous application of direct current and pressure. Powder is placed in electrically conductive die assembly with a uniaxial load applied by a top and bottom electrode, schematic shown in **FIGURE 3.3**. Current passes through the die assembly (and the sample if electrically conductive) to intimately and rapidly heat the sample at extremely high heating rates. Heating rates can be as high as 600 °C/min with cooling rates dependent on the systems individual cooling capabilities. The ability to rapidly reach temperature allows materials to dwell within the region where densification is dominant and can be cooled rapidly to produce nano-grained and non-equilibrium phases in metals and ceramics. Aside from the temperature response of the system, there are various SPS unique mechanisms that may contribute to the production of various materials with enhanced properties in comparison to radiative heating methods. These mechanisms include dielectric breakdown of surface oxides, electromigration effects that may enhance diffusion, and localized interparticle heating. "SPS" is the most common name for this kind of sintering technology, however, due to the various proposed sintering mechanisms, SPS technology can be referred to by various names throughout the research community: current-activated pressure assisted densification (CAPAD), pulsed electric current sintering (PECS), and field assisted sintering technology (FAST).

2.6 Finite Analysis Modeling of SPS

SPS is novel sintering technology only a couple of decades old. This has limited the technology to mostly lab-scale experimentation with few production companies using SPS technology. The main difficulty in producing large parts with SPS is the complexity

involved in reproducing uniformity. SPS is a current-assisted sintering technology that is highly dependent on tooling resistances and the electrical conductivity of the sample. Therefore, sample uniformity is governed by the current flow path within the tooling. During scale-up processing, electrical conductors like ZrB_2 experience massive overheating of the sample center and electrical insulators like Si_3N_4 have overheating on the sample edge. In order to circumvent an expensive trial-and-error approach to scale-up processing, there is growing interest in developing predictive computational models. Current models vary significantly with the focus of models being directed to describe specific SPS phenomena or fit to a specific manufacturer of SPS system. Models have been developed to describe both 3-dimensional and 2-dimensional environments. The entire sintering process is modeled with fit data or with a focus on the final stages of sintering at the dwell. There is also variation in the coupling of physics with thermal-electrical-mechanical models. Despite the multitude of models, there are very few that use the model as a tool to show the scale-up process or the development of complex shapes with experimental validation. In this dissertation we present guidelines into developing a finite element model that is supported with experimental data that shows the viability of using the model as a tool to predict temperature uniformity.

CHAPTER 3

Spark Plasma Sintering of Zirconium Diboride Using Carbon as an Oxide Reducing Agent. Part 1: Densification Behavior and Microstructural Analysis

3.1 Abstract Statement

ZrB_2 is processed with carbon additions to react with powder surface oxides in specific amounts based on predicted thermodynamic reactions. The resulting microstructure is characterized using STEM to identify a grain boundary chemistry composed of low melting metals of Co and Fe. In addition, discreet particle impurities of ZrO_2 are found with samples processed with carbon. It is not recommended to use carbon to maximize the reduction of ZrB2 surface oxides due to the formation of oxide based impurities in the microstructure.

3.2 Abstract

The effects of carbon as an oxygen reducing agent is investigated for spark plasma sintered ZrB_2. Oxygen content of the powder is measured after milling and after heat treatment to calculate the amount of oxygen from B_2O_3 and ZrO_2 – ZrB_2 is estimated to have 0.47 wt% oxygen from B_2O_3 and 0.47 wt% oxygen from ZrO_2. Carbon additions of 0.5 wt% and 0.75 wt% are used based on the estimated ZrO_2 content on the powder surface. Ball milled ZrB_2 and ZrB_2 with carbon additions were sintered at 1900 °C to >99% theoretical density. Carbon additions are shown to effectively remove powder surface oxides, however, after sintering, milled ZrB_2 and ZrB_2 with carbon additions contained microstructures with similar grain sizes of 9.1 ± 5.9 μm and 8.2 ± 5.1 μm, respectively.

Scanning transmission electron microscopy identified impurity phases composed of amorphous Zr-B-O with lamellar BN. ZrB_2 with carbon contained additional ZrO2 particle impurities and lamellar BN at grain boundaries.

3.3 Introduction

Borides, carbides and nitrides form the basis of transition metal ultra-high temperature ceramics (UHTCs), exhibiting melting temperatures in excess of 3000 °C [3]. Zirconium diboride (ZrB_2), has covalent and metallic bonding which gives it unique properties such as low density (6.09 g/cm^3), high strengths [10], and high thermal and electrical conductivity [11]. These properties have made ZrB_2 a UHTC of great interest for hypersonic applications and atmospheric re-entry vehicles as a refractory material for advanced composite thermal barrier protection materials in thermal protection systems (TPS) [2, 4]. However, there has been growing interest to develop a high purity ZrB_2 material in order to improve sinterability [7, 8, 12], and enhance high temperature mechanical [13] and thermal stability [14]. Methods to improve purity include additional powder processing steps to remove oxide impurities [15, 16] and to investigate new wet chemistry methods for synthesis of high purity and high surface area powders [6, 17, 18]. Oxides form on the ZrB_2 powder surface at room temperature according to the following thermodynamic reaction (Reaction 1):

$$ZrB_2 + {}^{5}/_{2}\, O_2 \rightarrow ZrO_2 + B_2O_3 \qquad (1)$$

These oxide impurities have been recognized to be the limiting factor in high temperature strengths of ZrB_2 UHTCs [13]. Previous work has shown powder heat treatment to be effective at removing surface B_2O_3 due to the high vapor pressure of the species from

1100-1500°C [19–21]. Through the addition of carbon and thermal treatment, ZrO_2 oxides can be targeted and reduced according the following thermodynamic reactions (Reactions 2-3):

$$ZrO_2 + B_2O_3 + 5C \rightarrow ZrB_2 + 5CO_{(g)} \quad (2)$$

$$ZrO_2 + 3C \rightarrow ZrC + 2CO_{(g)} \quad (3)$$

It is well known that reactive additives such as boron carbide (B_4C) and carbon [19, 22–24] promote the densification of ZrB_2 by removing surface oxides through the formation of volatile compounds or compounds that form a solid solution with ZrB_2 [25, 26]. Further, an excess amount of carbon is also used to minimize the oxygen in the powder system, which results in the formation of carbide contaminants or unreacted carbon that degrades mechanical properties [16, 24, 27].

We choose to use spark plasma sintering (SPS) to consolidate powders. SPS allows for the maximum versatility to process refractory ceramics due to the ability to control rapid heating and cooling rates which controls kinetics for grain growth and microstructure evolutions [28–31]. The rapid heating and cooling has been shown to be advantageous to create nanoscale microstructures [32, 33] and non-equilibrium and metastable phases [34, 35].

Scanning transmission electron microscopy (STEM) has been used to characterize the grain chemistry found in ZrB_2 and ZrB_2-based UHTC composites [36–38]. Grain boundary impurities were not found in the UHTC composites, however, Mizuguchi et. al [36] did show there was reduced oxygen detected at grain boundary interfaces in bulk ZrB_2 densified by SPS. Oxide phase impurities were not investigated and reducing agents were not used during the processing of these samples.

This work focuses on the effect of carbon as an oxygen reducing agent and its effects during densification using SPS. We propose using a processing method to determine the amount of oxides on the powder surface and the use of minimal carbon additions to remove the most oxides while minimizing the amount of impurity phases that can be formed from Reaction 3 during thermal treatment of the powder. We use SPS with rapid heating and cooling rates, and low pressure environment to promote thermodynamically favorable reactions and use STEM to investigate the impurities formed. The present work is Part 1 of a series that focuses on the processing and microstructure analysis of ZrB_2 densified using carbon additions and SPS. Part 2 will involve a CALPHAD assisted thermodynamic analysis of the possible reactions that form the impurities found in this work.

3.4 Experimental

3.4.1 Ceramic Powders

Commercially available zirconium diboride ([manufacturer reported impurities - C: 0.08wt%, O: 0.7wt%, N: 0.15wt%, Fe: 0.06wt%, Hf: 1.76wt%] grade B ZrB_2, H. C. Starck, Newton, MA) powder is used for this study. Oxygen and nitrogen from as-received powders are measured using the inert gas fusion method using infrared and thermal conductivity detection (ON736 Oxygen/Nitrogen Element Analyzer, LECO, St. Joseph, MI, USA) and carbon content measured using combustion analysis and infrared detection (CS744 Carbon/Sulfur Determinator, LECO, St. Joseph, MI, USA, services provided by NSL Analytical Services, Cleveland, OH). Powder specific surface area is measured (Autosorb-1, Quantachrome, Boynton Beach, FL) on powders before and after powder processing to determine particle size reduction using the Brunauer-Emmet-Teller (BET)

method [39]. Powder particle size, surface area, and chemical characterization is shown in **TABLE 3.1**.

The powder processing approach requires several steps as shown in the processing flow diagrams, **FIGURE 3.1**. The flow diagram can be separated into three key experimental components: 1) determine the amount of ZrO_2 on the powder and calculate the amount of carbon needed for reducing oxygen, 2) determine the carbon amount with the highest reaction efficiency after tube furnace thermal treatment, defined by a minimum carbon and oxygen content measured, and 3) densification of purified ZrB_2 powder using SPS.

3.4.2 Step 1: Powder Processing for Characterization Of ZrO_2 Impurities

As shown in **FIGURE 3.1a**, the as-received ZrB_2 powder is ball milled and oxygen content is measured to find the total oxygen contamination (B_2O_3+ZrO_2) on the powder surface. ZrB_2 is pre-heat treated in the tube furnace to evolve B_2O_3 and oxygen content is measured to determine the amount of ZrO_2 on the powder surface. Stoichiometric carbon additions are calculated based on the measured ZrO_2 after thermal treatment and Reaction 3.

Powder is ball milled for 24 hours at 150 RPM using 400 g of Co-bonded WC media (8mm satellites [18 vol% Co: 82 vol% WC], Union Process, Akron, OH) using 10 cm^3 batches of powder housed in 250 mL Nalgene bottles with 100 mL of hexane. Solvent from milled powder suspensions are rotary evaporated (IKA RV10 Digital, 2635 North Chase Parkway SE, Wilmington, NC) then granulated through a 150 μm sieve. WC contamination introduced by milling is estimated by weighing the media before and after

milling. Powder that is ball milled without the additions of carbon is referred to as BM-ZrB_2.

BM-ZrB_2 powder is pre-heat treated using a tube furnace (Astro A247, Thermal Technologies LC, Santa Rosa, CA) at 1500 °C for 1 hour to completely remove B_2O_3 from the powder surface, leaving only ZrO_2. The tube furnace is loaded with two zirconia boats lined with grafoil; one boat contains powder for heat treatment, located directly in the center of the furnace, while the second boat is filled with Ti sponge to act as a getter for the flowing argon (99.999% purity, Air Liquide, Plumsteadville, PA). The furnace is purged for 1 hour with argon at a flow rate of 6 cm/min at room temperature before loading the heat treatment program. The tube furnace temperature increases at a rate of 5 °C/min up to 1500 °C and held for 1 hour before cooling at a rate of 10 °C/min to room temperature. Milled powder without any carbon additions is referred to as BMHT1500-ZrB_2. After heat treatment, oxygen content drops to 0.47 wt%. Therefore, BM-ZrB_2 contains 0.47 wt% O from ZrO_2 and 0.47 wt% O from B_2O_3. Using Reaction 3, the stoichiometric amount of C needed to reduce ZrO_2 is approximately 0.50 wt% C.

3.4.3 Step 2: Powder Processing for Reaction Efficiency of Reducing Agent

As shown in **FIGURE 3.1b**, the next step includes processing BM-ZrB_2 with carbon additions and experimentally determine the minimum concentration of carbon additions that result in the least amount of residual carbon and oxygen impurities after heat treatment. Ball milled powder is processed using carbon additions at stoichiometry (0.50 wt% additive [+0 %]), and above stoichiometric additions (0.75 wt% additive [+50 %]) in order to investigate the reaction efficiency of our carbon source as a function of concentration, inside our tube furnace.

BM-ZrB_2 is processed using carbon additions in the form of phenolic resin (FD-2170, Borden Chemical Inc, Columbus, OH), with an experimentally derived char yield of 52.6%. BM-ZrB_2 (5 g – 0.8 cm^3), phenolic resin (0.0475g [0.5 wt%C] or 0.0713g [0.75 wt%C]), and 12 mL acetone (ACS Grade, BDH, Radnor, PA) are added to a 25 mL scintillation vial and mixed using a sonic horn with a 2.5 cm tip (Misonix S-4000, Qsonica llc, Newtown, CT) followed by rotary evaporation. The sonic horn used a 1 minute program with an ON-OFF pulse setting of 15 seconds ON, 5 seconds OFF, using a power amplitude of 1%.

Thermal gravimetric analysis and differential scanning calorimetry (TGA/DSC) using a high temperature Rh element furnace (Jupiter STA-449 F3, Netzch, Selb/Bavaria, Germany) under tube furnace temperature and flow conditions is used to identify when the reaction with carbon additions come to completion.

TABLE 3.1: ZrB_2 powder characteristics and oxygen and carbon content prior to SPS

Powder System	Particle Size (µm)	Surface Area (m^2/g)	Oxygen Content (wt%)	Carbon Content (wt%)
ZrB_2 As-received	2.6	1.0	0.25	0.08
ZrB_2 Ball Milled	1.5	4.51	0.94	0.25
ZrB_2 Ball Milled Heat Treated 1500°C (No Carbon)	1.5	4.51	0.47	0.04
ZrB_2+0.5 wt% Carbon	1.5	4.48	0.72	0.14
ZrB_2+0.75 wt% Carbon	1.5	4.48	0.47	0.04

3.4.4 Step 3: Powder Processing and Spark Plasma Sintering

Following **FIGURE 3.1c**, BM-ZrB_2 is processed with 0.75wt% carbon additions, heat treated in the tube furnace to reduce oxides, and finally densified using SPS. The final

sintering conditions are selected based on a density study using our control powder system, BM-ZrB_2 processed without carbon additions, that results in high density parts.

A SPS furnace (SPS 10-3 Thermal Technologies LLC, Santa Rosa, CA) with a maximum current capacity of 3000 A delivered on a 10 V rail with a 10 ton hydraulic press with a displacement resolution of 13 μm is used for densification. A pulsed direct current setting of 25 ms ON and 5 ms OFF is used to deliver current through the system, and the hydraulic press displacement is used to determine powder shrinkage profiles during densification.

The SPS control temperature is measured using a single color optical pyrometer (Marathon MM1MH, Raytek, Santa Cruz, CA) sighted on a hole drilled 7.5 mm into graphite die (Isocarb 85, Elctrodes Inc., Milford, CT). Graphite dies (50 mm outer diameter and 20 mm inner diameter) are lined with graphite foil (0.127mm thick (0.005in) Cupps Industrial Supply Inc., Tucson, AZ) and loaded with 4.6 g (0.75 cm^3) of powder to make 20 mm discs. Powder loaded dies are settled using a vibratory plate and pre-loaded using a standard press at 50 MPa for 1 min. Dies are thermally insulated using graphite felt wrapped ~15mm thick. A preload of 5 MPa and chamber vacuum level of 6 Pa is used prior to starting a run. A schematic of the SPS tooling configuration can be seen in Figure 3.a. SPS program uses an applied load from 5 MPa to 35 MPa at a rate of 30 MPa/min using an initial current load of 767 A until the pyrometer measures 600 °C. Direct current output is then controlled by the pyrometer temperature measurement and moderates the temperature ramp at a rate of 100°C/min to 1900°C with a 5 minute dwell through the use of a proportional-integral-derivative (PID) controller. Samples are cooled at a rate of

100°C/min to 1000°C and pressure is simultaneously ramped back down to 5 MPa at a rate of 30 MPa/min before current is shut off and the sample is allowed to cool naturally.

3.4.5 Bulk Chemical and Physical Property Characterization of Powders and Dense Ceramics

Powder samples of as-received ZrB_2, BM-ZrB_2, BMHT1500-ZrB_2, ZrB_2+0.5C, and ZrB_2+0.75C (minimum 1.0 g per element analyzed) are placed in a 10 mL scintillation vial and backfilled with Ar before being shipped for chemical analysis.

BM-ZrB_2, BMHT1500-ZrB_2, and ZrB_2+0.75C ceramic densities are measured using the Archimedes method with distilled water after SPS and graphite removal, in accordance with ASTM B311. Final theoretical densities (TD) are calculated using the densities of ZrB_2 as 6.09 g/cm^3 and Co-bonded WC as 14.9 g/cm^3. Oxygen and carbon content are measured on the dense ceramic parts. Samples prepared for elemental analysis are pulverized using a steel mortar and pestle to obtain particulates ranging from dust-like (~30 μm) to 1 mm. Neodymium magnets are used to remove any particles with steel contamination, loaded into 10 mL scintillation vials, backfilled with HP Ar, and shipped for measurement.

3.4.6 Bulk Microstructure and Grain Size Analysis of Ceramics

Ceramics are prepared for microstructure and grain size analysis by polishing discs with a progression of polishing pads: 120 grit diamond, 220 grit diamond, 40 μm diamond, 25 μm diamond, and mirror finishing with 1200 grit silicon carbide. A field emission scanning electron microscope (S-4800 Field Emission Scanning Electron Microscope, Hitachi Inc, Pleasanton, CA) equipped with energy dispersive X-Ray spectroscopy capabilities (NORAN™ System Six X-ray Microanalysis System, Thermo Scientific,

USA) is used for microstructural analysis, including grain size and impurity particle detection. SEM samples are examined using secondary electrons at 15 kV and 10 μA collected through the objective lens in the upper detector. For grain size measurements, mirror polished samples undergo wet chemical etching with molten NaOH at 500 °C for 7 seconds in a graphite crucible on a hot plate followed by a distilled water quench. SEM micrographs for grain size analysis are measured using Image J (Image J 1.44o, National Institute of Health, Bethesda, MD) imaging software reporting the maximum ferret diameter – several SEM images are used to obtain a minimum of 200 counted grains per composition.

TABLE 3.2: ZrB_2 chemical characterization and density after SPS at 1900°C with a 5 minute dwell as a function of powder processing.

Powder System	Oxygen Content After SPS (wt%)	Carbon Content After SPS (wt%)	Onset of Densification	Theoretical Density	Density (g/cm^3)	Grain Size (μm)
ZrB_2-BM	0.18	0.007	1000°C	99.6%	6.11	9.0 ± 5.9
ZrB_2-HT1500 (no carbon)	0.24	0.005	1525°C	93.4%	5.73	5.2± 3.4
ZrB_2+0.75wt%C	0.12	0.036	1375°C	100.2%	6.15	8.2± 5.1

3.4.7 Stem Specimen Preparation, Characterization and Analysis

Samples of BM-ZrB_2 and ZrB_2+0.75C sintered discs are prepared into machined coupons (1.5 mm x 2.0 mm x 0.5 mm) for STEM specimen preparation. The coupons are then mechanically polished to electron transparency using an Allied Multiprep^{TM}. Samples for STEM are then further thinned using a Fischione 1050 argon ion mill operated using energies between 200 eV and 2 keV with LN_2 cooling of the sample.

Specimens are examined using a 200 kV C_s probe-corrected FEI Titan G2 60-300 kV TEM/STEM equipped with a high brightness X-FEG electron source, a Super-X detector for energy dispersive X-ray spectroscopy (EDS). Data acquisition and post processing of the EDS data is performed using Bruker Espirit software. The characteristic K lines are used for mapping every element other than W, which uses the L lines. Twenty high angle annular dark-field (HAADF) images covering an approximate area of 100 μm^2 are acquired to provide a large sampling size for microstructural characterization on each system.

3.5 Results and Discussion

3.5.1 Effects of Ball Milling and Densification Behavior and Grain Size

Ball milling introduces 0.54 vol% media contamination to the powder. Media contamination translates to an introduction of 0.09 vol% cobalt and 0.44 vol% WC. BM-ZrB_2 has a reduced particle size from the as-received source and specific surface area is increased from 1.0 m^2/g to 4.5 m^2/g, which increased oxygen and carbon contamination to 0.94 wt%O and 0.27 wt%C. WC contamination is estimated to contribute less than 0.01 wt% carbon, therefore, the majority of the carbon contamination detected on BM-ZrB_2 is attributed to adsorbed solvent. This solvent is shown to evaporate at 500 °C, presented in the TGA/DSC data (**FIGURE 3.2**). Two additional distinct DSC signals are detected at 1150 °C (Reaction 2) and 1500 °C (Reaction 3). ZrB_2+0.75C has the highest reaction efficiency which resulted in the least amount of oxygen and carbon contamination after tube furnace treatment. ZrB_2+0.5C is based on a stoichiometric addition of carbon based on Reaction 3, however, oxygen and carbon analysis after powder heat treatment shows significant oxygen and carbon retained on the surface powder. The reaction temperatures found using

TGA and the oxygen and carbon content on ZrB_2+0.5C will be discussed in further detail in Part 2 of this work. A summary of ZrB_2 powder physical and bulk chemical characteristics are listed in **TABLE 2.1** for 1) as-received ZrB_2, 2) ball milled ZrB_2 (BM-ZrB_2), 3) ball milled and heat treated at 1500°C (BMHT1500-ZrB_2), and 4) ball milled and heat treated with carbon additions at 1500°C (ZrB_2+0.5C and ZrB_2+0.75C).

After powder processing and heat treatment in the tube furnace, powders are densified in the SPS. A summary of chemical and physical characterizations of BM-ZrB_2, BMHT1500-ZrB_2 and ZrB_2+0.75C after SPS can be seen in **TABLE 2.2**, showing a decrease in oxygen content with carbon additions. ZrB_2+0.75C measured carbon content before and after SPS are the same. The retained carbon after SPS indicates the reaction process was completed in the tube furnace, as continued reaction in the SPS (Reaction 2 and 3) would form CO gas that would lower the total carbon content in the system. After SPS, ZrB_2+0.75C oxygen is further reduced. This reduction may be attributed to SPS unique phenomena such as dielectric breakdown of oxides [40] which has also been noted in previous work [16].

In situ shrinkage profiles for BM-ZrB_2, BMHT1500-ZrB_2 and ZrB_2+0.75C powders densified at 1900°C-5min are shown in **FIGURE 3.3b**. BM-ZrB_2 powders show an early onset of densification starting at 1100°C, which is not an active phase of densification. Rather, it is attributed to coarsening mechanisms that minimizes surface area energy without particle centers moving closer together. This vapor transport mechanism is known inhibit densification by allowing rapid grain growth [15, 41, 42] below densification temperatures. The temperature regime for ZrB_2 densification is shown in the shaded region on the shrinkage curves in **FIGURE 3.3b**. BM-ZrB_2 has average grain size of 9.0 ± 5.9 μm

with an oxygen content of 0.18 wt% after SPS. The shrinkage plot for BMHT1500-ZrB_2 exhibits a delayed onset of densification starting at 1525 °C and a reduced shrinkage rate, compared to BM-ZrB_2, which is attributed to the reduced boria content from thermal treatment. After SPS, BMHT1500-ZrB_2 has a relative density of 93%, an average grain size of 5.2 ± 3.4 μm and 0.24 wt% oxygen content. Thus, if a low oxide, small grained microstructure is desired, then B_2O_3 should be removed from the powder prior to SPS. Likewise, ZrO_2 should be removed to further reduce oxygen content and enable densification.

The shrinkage plot for ZrB_2+0.75C has an onset of densification at 1400°C, without the low temperature shrinkage characteristics of B_2O_3. The final ceramic achieves 100% relative density with a grain size of 8.2 ± 5.1 μm and 0.12 wt% oxygen content after SPS. After SPS, it is evident there is only minor reduction in oxygen content and grain sizes are statistically similar to BM-ZrB_2. Based on Reaction 2 and 3, oxygen content should have been reduced further and will be addressed in Part 2 of this study.

3.5.2 Microstructural Analysis Using SEM and STEM

Microstructural analysis shows impurity particles within both BM-ZrB_2 and ZrB_2+0.75C ceramics. **FIGURE 3.4a** shows BM-ZrB_2 SEM microstructures with oxide phases ranging from 0.7 – 1.5 μm in diameter within the grain boundaries. EDS analysis indicates they contain Zr and B, with some phases containing N (lighter shade phase). SEM microstructures for ZrB_2+0.75C (**FIGURE 3.4c**) also contain oxide phases, but much smaller in size, with a diameter range of 0.2 - 0.6 μm. The microstructure also shows boron-nitrogen impurities segregated at the grain boundaries and carbide contamination, which are differentiated from oxides by EDS point analysis.

In order to determine the differences in structure of these impurity phases at the grain boundaries, STEM analysis is performed. STEM identified intragranular oxides in BM-ZrB_2 (**FIGURE 3.4b**) that may develop due to the high initial oxygen content of the powder as it enters the SPS. STEM analysis of ZrB_2+0.75C oxide phases shows an additional oxide impurity in the form of discreet ZrO_2 particles. Nitrogen impurities are found to exist outside of the oxide phase and pinned at the grain boundaries. The formation of nitrogen impurities is most likely caused by the initial presence of N pre-existing in the powder. Element analysis confirms a nitrogen content of 0.19 wt% in the powder. Others have analyzed ZrB_2 powder under TEM to reveal an even distribution of N contamination on the powder surface which was determined to be cubic-BN and BN_xO_y[43]. As the oxide size decreases, lamellar BN precipitates in between grain boundaries, as found in ZrB_2+0.75C. Further analysis needs to be performed to identify the formation of the BN filaments found in both BM-ZrB_2 and ZrB_2+0.75C microstructures.

3.5.3 Analysis of Interparticle Impurities and Grain Boundary Phase Chemistries

BM-ZrB_2 has a high oxygen content after SPS, and STEM analysis of the oxide phases shows they are primarily comprised of layered boron nitride surrounded by an amorphous Zr-B oxide layer using HAADF and EDS (**FIGURE 3.5a**). Phases formed at the triple points contain traces of manufacturer powder impurities, such as Ag, Ca, Al, and Y. Low melting temperature metals, Co and Fe, were found to segregate to the grain boundaries for each sample, as shown in the STEM grain boundary analysis in **FIGURE 3.5b**, with W forming a solid solution with ZrB_2 shown in **FIGURE 3.6**. Spectroscopic investigation of ZrB_2+0.75C (**FIGURE 3.7a**) shows oxides are composed of a mixture of boron nitride, amorphous Zr-B oxide, and particles of free carbon. Grain boundaries

contain Co and Fe in addition to zirconium oxide particles, seen in **FIGURE 3.7b**. The presence of low melting temperature species at the grain boundaries is concerning as they may be detrimental to high temperature mechanical properties when tested.

3.6 Summary and Conclusion

The purpose of this study was to investigate the effects of carbon as an oxide reducing agent for ZrB_2 densified using SPS and analyze the microstructure impurities that are formed using SEM and STEM. All samples were densified under the same SPS conditions with an applied uniaxial load of 30 MPa, die wall temperature of 1900 °C with a 5 minute dwell time. BM-ZrB_2 and ZrB_2+0.75C obtained near 100% theoretical density. Carbon additions were shown to be effective at removing oxides on the powder surface, however, they were not effective at removing oxygen during SPS. Grain sizes for BM-ZrB_2 and ZrB_2+0.75C are statistically similar at 9.1 ± 5.9 μm and 8.2 ± 5.1 μm, respectively.

SEM and STEM showed that both powder systems contained an amorphous Zr-B oxide phase accompanied by a lamellar BN. ZrB_2+0.75C was shown to include discreet particle impurities of lamellar BN pinned between the grain boundaries and ZrO_2 in the grain boundaries. Tungsten was found to be in solid solution with the ZrB_2 matrix and cobalt segregating at the grain boundary interface, which are products from milling media contamination. The presence of Co and Fe at the grain boundary interface may be detrimental to high temperature mechanical properties due to their low melting temperature. Carbon is not recommended as an oxide reducing agent due to the presence of oxide based impurities found in the grain boundaries.

3.7 Acknowledgements

A National Science Foundation Early Faculty Career Award under Division of Materials Research-0954110 supports material processing of ceramics using spark plasma sintering. Support for this work by the National Science Foundation Graduate Research Fellowship (Grant DGE-1252376) is also appreciated. The authors acknowledge the use of the Analytical Instrumentation Facility (AIF) at North Carolina State University, which is supported by the State of North Carolina and the National Science Foundation.

3.8 Figures

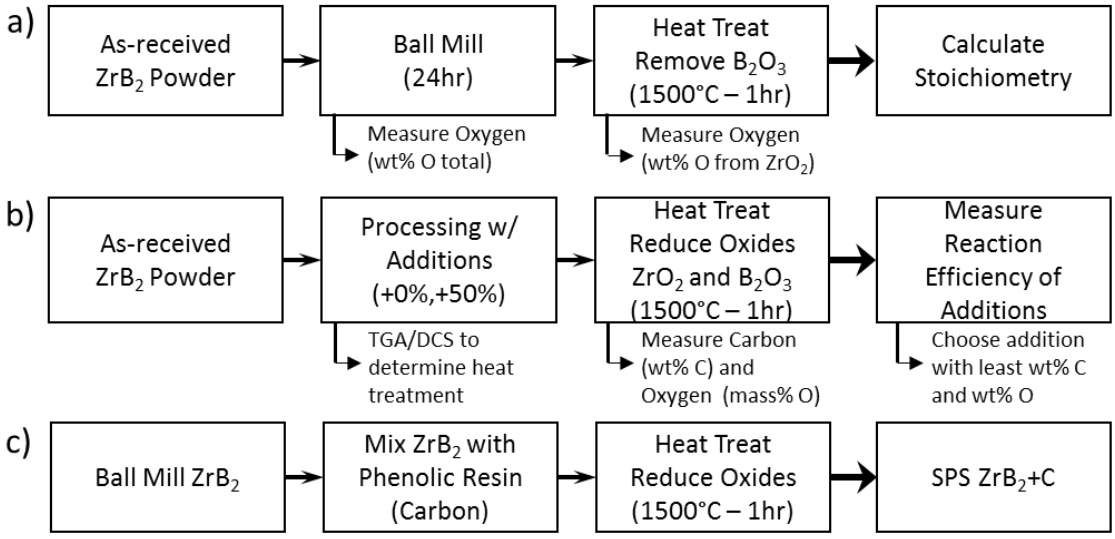

FIGURE 3.1: Processing schematics are shown to a) determine the amount of ZrO_2 on the powder after milling, b) process the powder with additions below stoichiometry, at stoichiometry, and above stoichiometry to determine the thermodynamic efficiency of the reaction based on residual carbon measured, and c) using the most efficient addition to SPS to produce ultra-high purity ZrB_2.

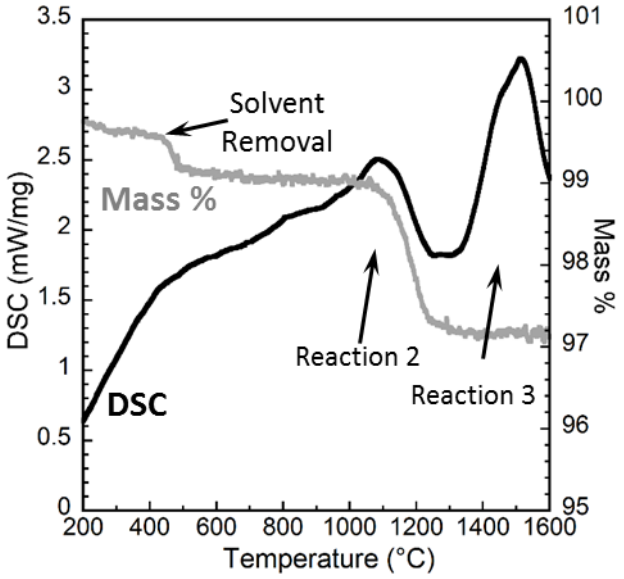

FIGURE 3.2: TGA/DSC data is presented for ZrB_2+C. ZrB_2+C has observable reactions at 1100°C and 1500°C. By the end of the run, mass is stabilized, indicating the reaction has come to completion.

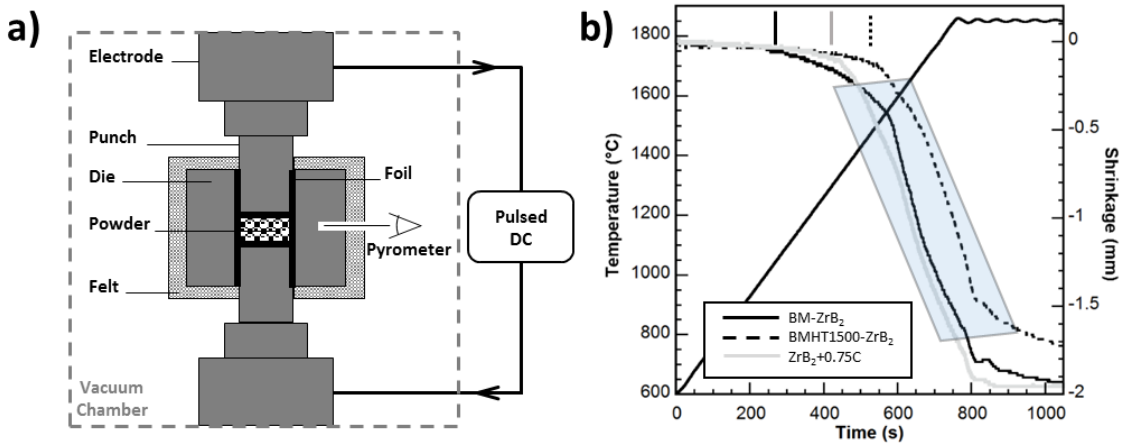

FIGURE 3.3: a) SPS tooling schematic showing how pulsed current flows through the graphite tooling, internal grafoil wrapping, external graphite felt thermal insulation and the pyrometer sighting location. b) Shrinkage profiles for ZrB_2 densified at 1900 °C for 5 minutes are shown for BM-ZrB_2, BMHT1500-ZrB_2 and ZrB_2+0.75C. The temperature in which densification begins is noted by the vertical lines. BM-ZrB_2 shows signs of early shrinkage attributed to high B_2O_3 content.

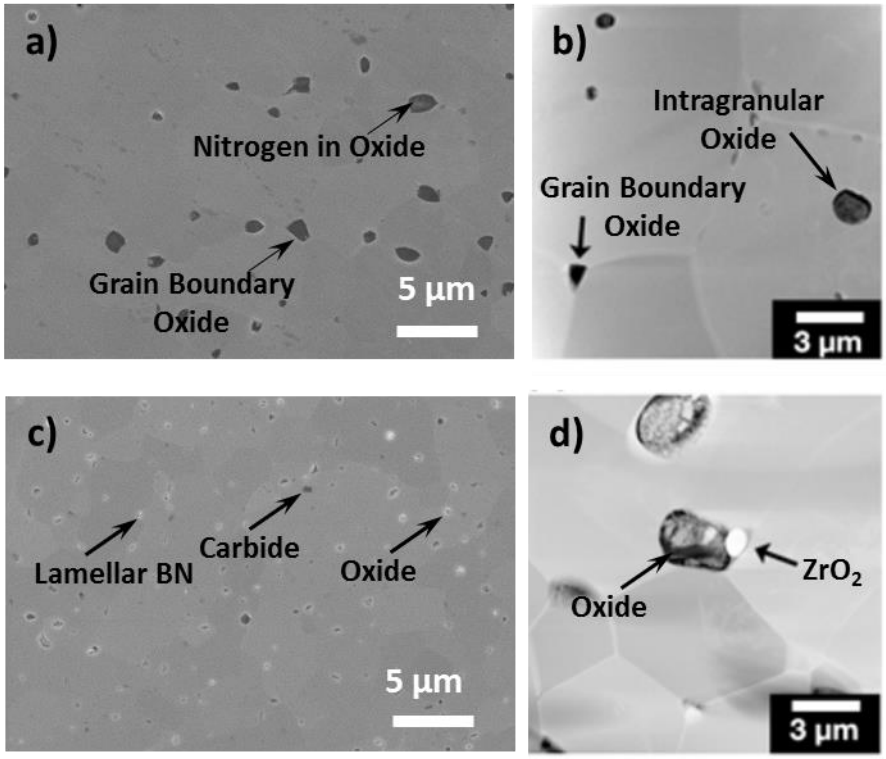

FIGURE 3.4: Microstructures of BM-ZrB_2 through a) SEM and b) TEM imaging show both grain boundary oxides and intragranular oxide impurities due to the high initial oxygen content of the powder. Microstructures of ZrB_2+0.75C through c) SEM show a decrease in the oxide impurity size with the introduction of lamellar BN at grain boundaries and minor carbide impurities. d) STEM imaging reveals discreet ZrO_2 particles in the microstructure.

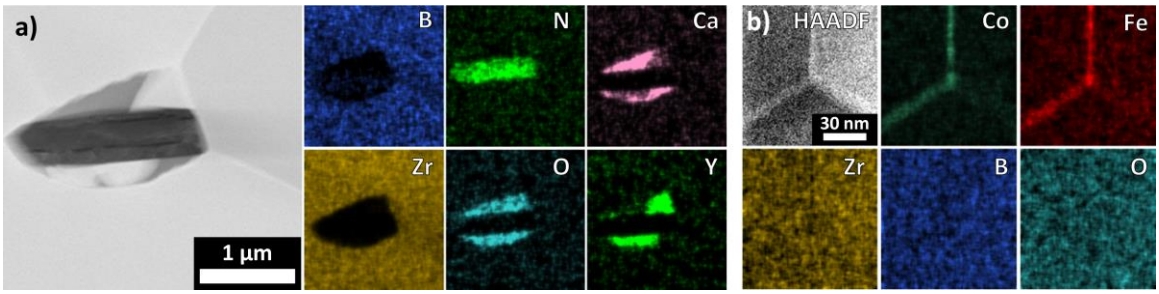

FIGURE 3.5: STEM analysis is shown for ZrB_2-BM **a)** interparticle impurities and **b)** typical grain boundary chemistry. **a)** BM-ZrB_2 contains an amorphous Zr-B-O oxide that can be enveloped in a BN layered structure. **b)** Grain boundaries are typically composed of low melting Co and Fe.

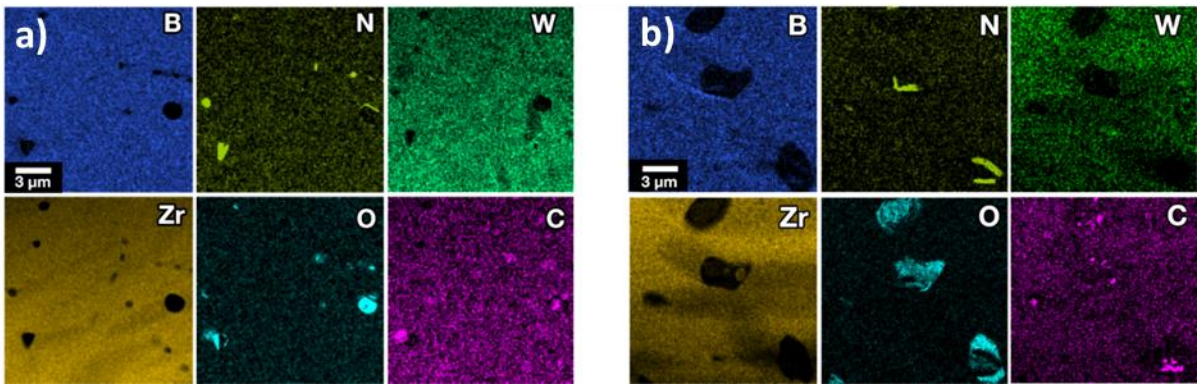

FIGURE 3.6: SEM and STEM spectroscopic analysis with EDS maps are shown for a) ZrB_2-BM and b) ZrB_2+0.75 wt%C. Due to the high volume of impurities in BM-ZrB_2, oxides composed of B_2O_3 and ZrO_2 become trapped within the grain boundaries and diffuse into the grain to form intragranular oxides. Due to the low thermodynamic efficiency to reduce ZrO_2 using carbon, a high degree of impurities remain, and excess carbon can be seen in the oxide envelopes.

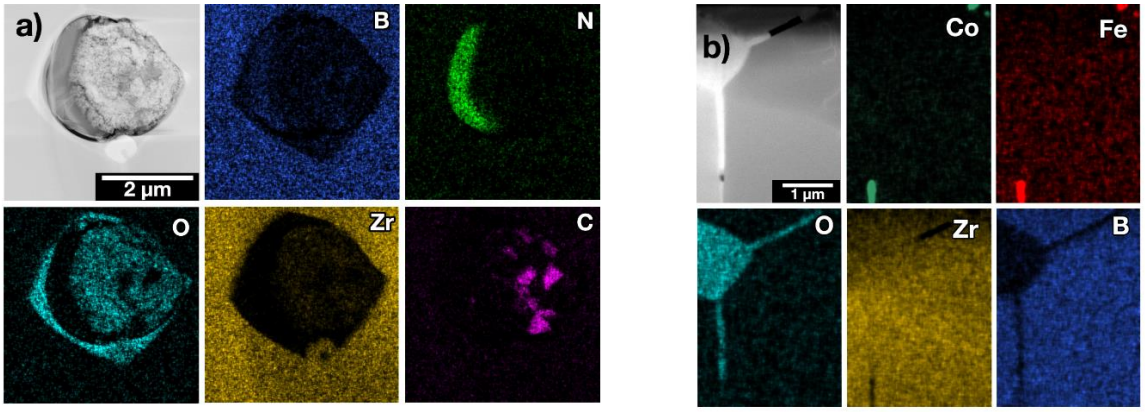

FIGURE 3.7: STEM analysis of ZrB_2+C is shown. a) ZrB_2+C impurities contain Zr-B-O amorphous oxides with free carbon surrounded by a layered BN and discreet ZrO_2 particles. b) ZrB_2+C grain boundaries contain oxide particle impurities.

CHAPTER 4

Spark Plasma Sintering of Zirconium Diboride Using Carbon as an Oxide Reducing Agent. Part 2: Thermodynamic Analysis of Impurity Phases

4.1 Abstract Statement

The first thermodynamic model for the Zr-C-O system was developed to predict the microstructures found in ZrB_2 processed with carbon. ZrO_2-C pseudo binary and Zr-C-O ternary phase equilibria were calculated to show how carbon as an oxide reducing agent prevents complete oxide removal through the formation of zirconium oxycarbides. Even if excess carbon additions are used, oxygen will still remain in the system in the form of ZrC_xO_y with a low oxygen content. Through the development of the thermodynamic model, it can be extended to incorporate similar metal diboride systems of hafnium and titanium that will allow for an extensive thermodynamic analysis to predict microstructures prior to processing and densification.

4.2 Abstract

ZrB_2 is processed with carbon additions to reduce surface oxide concentrations prior to densification using spark plasma sintering. A CALPHAD-based thermodynamic model of the Zr-C-O system is used to evaluate and predict oxide impurity formation before and after SPS. The thermodynamic model predicts the direct reaction of ZrO_2 and C will form a zirconium oxycarbide (ZrCxOy). The Zr-C-O ternary model predicts ZrC_xO_y can retain up to 10 mol% oxygen when ZrC is in equilibrium with ZrO_2 and a minimum of 0.1

mol% oxygen when ZrC is in equlibrium with carbon. ZrO_2 particle impurities are proposed to precipitate from the dissolution of C from ZrC_xO_y into ZrB_2.

4.3 Introduction

Over the past two decades, spark plasma sintering (SPS) has become an increasingly attractive method to produce materials to high density with limited grain growth and desirable properties over conventional sintering methods like the hot press (HP) [28–31]. Through rapid powder consolidation, microstructures are able to maintain their grain size producing nanoscale microstructures [32, 33, 44, 45]. SPS mechanisms that have been shown to help produce desirable properties include the rapid heating rates (up to 300°C/min) [46] which can produce localized interparticle heating [47], and sample exposure to current density[48], which can influence dielectric breakdown of surface oxides [49–51] and extreme interparticle heating [52].

Benefits of SPS grain size retention has also been noted with ZrB_2-based ultrahigh tempera-ture ceramics [20, 30]. Unfortunately due to the enhanced densification capabilities of SPS, mechanical properties of SPS sintered and HP parts can vary significantly due to the numerous powder processing methods employed [53–55]. When comparing ZrB_2 ceramics consolidated with SPS and HP that resulted in similar grain size and oxygen impurity content, SPS produced ceramics showed improved room temperature mechanical properties [56].

In a previous study, ZrB_2 was processed with the additions of carbon to reduce surface oxides [57]. ZrB_2 with carbon was heat treated in a tube furnace to reduce surface oxides according to the following reactions:

$$ZrO_2 + B_2O_3 + 5C \rightarrow ZrB_2 + 5CO_{(g)} \quad (1)$$

$$ZrO_2 + 3C \rightarrow ZrC + 2CO_{(g)} \quad (2)$$

Tube furnace heat treatment enabled the reactions and reduced powder surface oxides. However, after SPS, oxygen content was measured and the resulting part did not show significant oxygen reduction. Rather, microstructures contained impurity phases of discreet ZrO_2 particles and amorphous Zr-B-O phases.

Currently there is no thermodynamic model available commercially or in literature that can evaluate all the possible reactions when reducing ZrO_2 with carbon. Computational models in the current literature do not provide information about the solubility of oxygen in ZrC, thus making it necessary to develop a new model. In this study, we use a CALPHAD-based thermodynamic model of the Zr-C-O system to predict the formation of the impurity phases before and after SPS.

4.4 Experimental

4.4.1 Ceramic Powders and Powder Processing

For this study, commercially available zirconium diboride powder ([manufacturer reported impurities - C: 0.08wt%, O: 0.7wt%, N: 0.15wt%, Fe: 0.06wt%, Hf: 1.76wt%] grade B ZrB_2, H. C. Starck, Newton, MA) and phenolic resin (FD-2170, Borden Chemical Inc, Columbus, OH) are used. ZrB_2 is ball milled with cobalt bonded tungsten carbide media (8mm satellites [18 vol% Co: 82 vol% WC], Union Process, Akron, OH) in hexane. The powder suspension is dried using a rotary evaporator (IKA RV10 Digital, 2635 North Chase Parkway SE, Wilmington, NC) and granulated using a 150 μm sieve – the resulting powder system is referred to as BM-ZrB_2.

BM-ZrB_2 is combined with acetone and phenolic resin to yield either 0.5 wt% or 0.75 wt% carbon and mixed using a sonic horn (2.5 cm tip ,Misonix S-4000, Qsonica llc, Newtown, CT). The slurry is rotary evaporated and sieved – the resulting powder systems are referred to as ZrB_2+0.5C and ZrB_2+0.75C. ZrB_2 with carbon is heat treated using a tube furnace (Astro A247, Thermal Technologies LC, Santa Rosa, CA) at 1500 °C for 1 hour with flowing argon gas (99.999% purity, Air Liquide, Plumsteadville, PA). Thermal gravimetric analysis and differential scanning calorimetry (TGA/DSC) using a high temperature Rh element furnace (Jupiter STA-449 F3, Netzch, Selb/Bavaria, Germany) under tube furnace temperature and flow conditions is used to identify when the reaction with carbon additions come to completion, shown in **FIGURE 4.1**.

4.4.2 Spark Plasma Sintering (SPS)

BM-ZrB_2 and ZrB_2+0.75C is densified using an SPS furnace (SPS 10-3 Thermal Technologies LLC, Santa Rosa, CA). Powder is loaded in an electrically conductive graphite die (Isocarb 85, Elctrodes Inc., Milford, CT) to make 20mm discs 3.5mm thick. The sintering is performed at 1900 °C and 35MPa with a dwell time of 5 minutes under vacuum (~6 Pa). Samples are heated at a rate of 100 °C/min up to the sintering temperature and cooled at 100 °C/min to 1000 °C and allowed to cool naturally. A detailed procedure for powder processing and SPS tooling can be found in previous work [57].

4.4.3 CALPHAD-Based Thermodynamic Model for The Ternary Zr-C-O

The zirconium-carbon-oxygen ternary phase equilibrium system at elevated temperatures is created using Thermo-Calc (Thermo-Calc Software AB, version 3.01.1, Stockholm, Sweden) via the CALPHAD method, which describes all available phase equilibria and thermochemical properties through Gibbs free energy and adjustable

parameters to accurately fit data. Existing models that describe the binary systems Zr-C [58], Zr-O [59], and C-O are used as the foundation of this preliminary model. Experimental data for the solubility of oxygen in ZrC from Sarkar et al. [60] is appended into the databases through the adjustment of thermodynamic parameters for the Zr-C-O ternary interaction. The current model omits the addition of configurational entropy during the parameterization of the model, therefore, the oxygen solubility reported using the model are a maximum representation. The Zr-C-O model is used to provide insight into the reduction reaction of ZrO_2 and C in the tube furnace and possible reaction routes during SPS processing.

4.5 Results and Discussion

4.5.1 TGA and Tube Furnace Reaction Analysis

TGA data is plotted as a function of time, and shows two distinct weight loss regions, shown in **FIGURE 4.1**. Weight loss begins at 1170 °C and with a lower weight loss at 1400 °C. Reaction 1 is thermodynamically favorable at 1490 °C in standard atmosphere (101 MPa) and has been shown to be favorable as low as 1035°C under a low pressure environment of 13 Pa [24]. Similarly, Reaction 2 is thermodynamically favorable at 1637 °C under standard atmospheric conditions and becomes increasingly favorable at lower temperatures with decreasing pressure. It must be noted that phase diagrams work under a closed system and most experiments are performed in open systems, thus, assumptions have to be made when using phase diagrams. Although the actual tube furnace conditions may be under atmospheric pressure, the reactions are driven by the partial pressure of $CO_{(g)}$ in the system. In order to understand the environment in the tube furnace and TGA that allows for these reactions to occur at low temperature, several pseudo-binary phase

diagrams of the ZrO_2-C system are plotted as a function of pressure. **FIGURE 4.2a** under standard atmospheric conditions confirms that that ZrO_2 and C do not react until 1637 °C. With decreasing pressure the reaction becomes more favorable. The actual tube furnace pressure must be below 0.2 atm, according to the ZrO_2-C phase diagram in **FIGURE 4.2c** and reaction temperatures from TGA data. Under these low pressures, it is possible for B_2O_3 on the powder surface to evolve as gas species [21, 25]. Thus Reaction 1 would be limited by the vaporization rate of B_2O_3 and carbon will react directly with ZrO_2 according to Reaction 2.

In Part 1 of this study, ZrB_2 was heat treated in the tube furnace with 0.5 wt% and 0.75 wt% carbon additions. ZrB_2+0.5C after reacting in the tube furnace contained 0.72 wt% oxygen and 0.14 wt% carbon while ZrB_2+0.75C contained 0.47 wt% oxygen and 0.04 wt% carbon. From **FIGURE 4.2d**, it is shown that there is a miscibility gap in the ZrC phase associated with oxygen retention in an oxycarbide phase of ZrC_xO_y [61]. Due to the minor amounts of carbon added to the powder to enable the reaction, carbides could not be detected with either EDS or XRD analysis. However, the measured carbon content in ZrB_2+0.75C (total carbon after SPS: 0.04 wt%) suggests there are carbides and carbon in the microstructure in comparison to BM-ZrB_2 with a carbon content <0.01wt%. In addition, the phase diagram predicts the formation of a ZrC_xO_y phase and shows with decreasing pressure, there is greater retention of oxygen in the ZrC phase at 1500°C. With precise control of environment and temperature, the ZrO_2-C phase diagrams predict the ability to produce ZrC without oxygen contamination. In **FIGURE 4.2d**, for example, the ZrO_2 and C reaction must be limited to 1438°C to minimize oxygen solubility in ZrC, however as this is the minimum temperature for the reaction, long reaction times should be

expected. The formation of ZrC_xO_y can explain why the tube furnace treatment does not allow for complete removal of oxygen, however, it cannot account for the excessive carbon measured in ZrB_2+0.5C, which may be a kinetics related problem.

FIGURE 4.3 can be used to summarize the powder heat treatment process based on the above analysis. In **FIGURE 4.3b**, BM-ZrB_2 is coated with B_2O_3 and ZrO_2. With the addition of carbon (**FIGURE 4.3c**), and tube furnace treatment, B_2O_3 evolves and carbon reacts with ZrO_2 to form ZrC_xO_y as shown in the reaction below:

$$ZrO_2 + (2 + x - y)C \rightarrow ZrC_xO_y + (2 - y)CO_{(g)} \qquad (3)$$

At this stage the oxygen content is determined by the equilibrium states ZrC/C and ZrC/ZrO_2. If carbon is in equilibrium with ZrC, ZrC can retain up 0.25 mol% oxygen. Conversely, if ZrC is in equilibrium with ZrO_2, it can retain a maximum of 7.9 mol% oxygen.

4.5.2 Impurity Analysis After SPS

After SPS, STEM analysis found impurities composed of an amorphous Zr-B-O and discreet ZrO_2 particles. The preliminary thermodynamic model used in this study does not contain any B species and cannot be used to discuss the formation of these impurities. However, the formation of amorphous Zr-B-O can be identified through by using a ZrO_2-B_2O_3 binary phase diagram from literature and proposed liquid oxide reaction [62]:

$$ZrB_2 + \frac{5}{2}O_2 \rightarrow (1 - x)(ZrO_2)_{cr} + (B_2O_3 + xZrO_2)_{liq} \qquad (4)$$

The ZrB_2-B_2O_3 phase diagram shows up to 10 mol% ZrO_2 can form a liquid with B_2O_3 at 1400 °C. This solubility can increase up to 50 mol% ZrO_2 at 1900 °C and is likely

to increase with low pressure. The Zr-B-O solubility may also be the reason for the incomplete evolution of B_2O_3 during tube furnace treatment. Due to the rapid heating and cooling rate of SPS, it is possible to form the Zr-B-O phase during sintering and rapid cooling prevents the dissociation of discreet ZrO_2 and B_2O_3 phases.

Microstructure analysis of ZrB_2+0.75C shows discreet ZrO_2 particles at grain boundaries, triple points and alongside the amorphous Zr-B-O phase, grain boundary ZrO_2 can be seen in **FIGURE 4.4**. The formation of ZrO_2 particle impurities is evaluated using the Zr-C-O ternary phase diagram under SPS temperature and pressure conditions, shown in **FIGURE 4.5a**. The ZrC/ZrO_2 equilibrium shows an increase in oxygen solubility up to 10 mol% oxygen. Therefore, during SPS, it is unlikely that ZrC_xO_y precipitates ZrO_2 particles due to the increased oxygen solubility. The ZrC/C equlibrium shows decreased oxygen with an oxygen solubility of 0.1mol%. If ZrC/C are in equilibrium during SPS, the resulting products would form $CO_{(g)}$ and not discreet ZrO_2 particles.

During processing of ZrB_2+0.75C, the phenolic resin uniformly coats the particles surfaces and forms ZrC_xO_y particles during heat treatment in the tube furnace. Carbon has a maximum solubility of 2 mol% in ZrB_2 at 2400°C [63]. Thus, during SPS, the Zr(C,O) can form ZrO_2 particles through the following proposed thermodynamic reaction:

$$ZrB_2 + ZrC_xO_y \rightarrow ZrB_{2-x}C_x + ZrO_y + B_{x(l)} \qquad (5)$$

Through the solubility of carbon in ZrB_2, discreet ZrO_2 particles can form throughout the microstructure. The formation of discreet ZrO_2 particles is expected to be a result of abnormally high interparticle temperatures that can be obtained using SPS [40, 49,

[52], and work is on-going to determine the effects of sample current density on the oxide structure of ZrB_2 ceramics.

FIGURE 4.5 can be used to summarize the impurities formed during SPS. BM-ZrB_2 with its high oxygen content evolves a large volume of oxides during SPS, **FIGURE 4.5b**. As a result, oxides become trapped at grain boundaries and inside the grains. By using carbon additions and powder heat treatment prior to SPS, the amount of oxides is reduced. However, due to the expected formation of ZrC_xO_y during tube furnace treatment and high interparticle temperatures during SPS, carbon is dissolved into the ZrB_2 matrix and discreet ZrO_2 particles precipitate, **FIGURE 4.5c**. Due to the solubility of oxygen in ZrC, carbon is not an effective oxide reducing agent.

4.6 Summary and Conclusion

The purpose of this study was to investigate the formation of impurities of ZrB_2 processed with carbon and densified using SPS. Impurity formation was aided by the use of a preliminary thermodynamic model of the Zr-C-O system. We developed the first Zr-C-O thermodynamic model to predict microstructure impurities through the development of phase equilibria diagrams. ZrO_2-C pseudo binaries were modeled showing the direct reaction of ZrO_2 and C becomes increasingly favorable with decreasing pressure. The thermodynamic model predicts ZrO_2 and C to form a ZrC phase with oxygen solubility, zirconium oxycarbide (ZrC_xO_y). Although we were unable to directly detect the oxycarbide in the powder, the phase diagram and measured carbon content suggests it forms during tube furnace heat treatment. In addition, discreet ZrO_2 particle impurities in ZrB_2 processed with carbon are expected form due to the solubility of carbon in ZrB2 that dissociates ZrC_xO_y into ZrO_2 during SPS.

4.7 Acknowledgements

A National Science Foundation Early Faculty Career Award under Division of Materials Research-0954110 supports material processing of ceramics using spark plasma sintering.

4.8 Figures

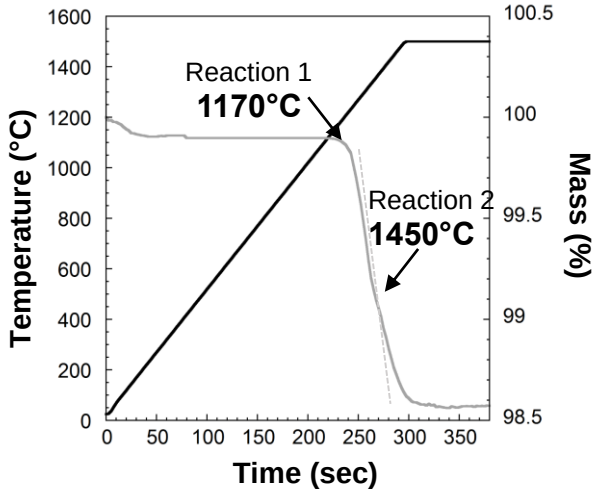

FIGURE 4.1: TGA/DSC data is presented for ZrB_2+C as a function of time. Two distinct weight loss regimes are identified at 1170°C associated with Reaction 1 and at 1450°C associated with Reaction 2.

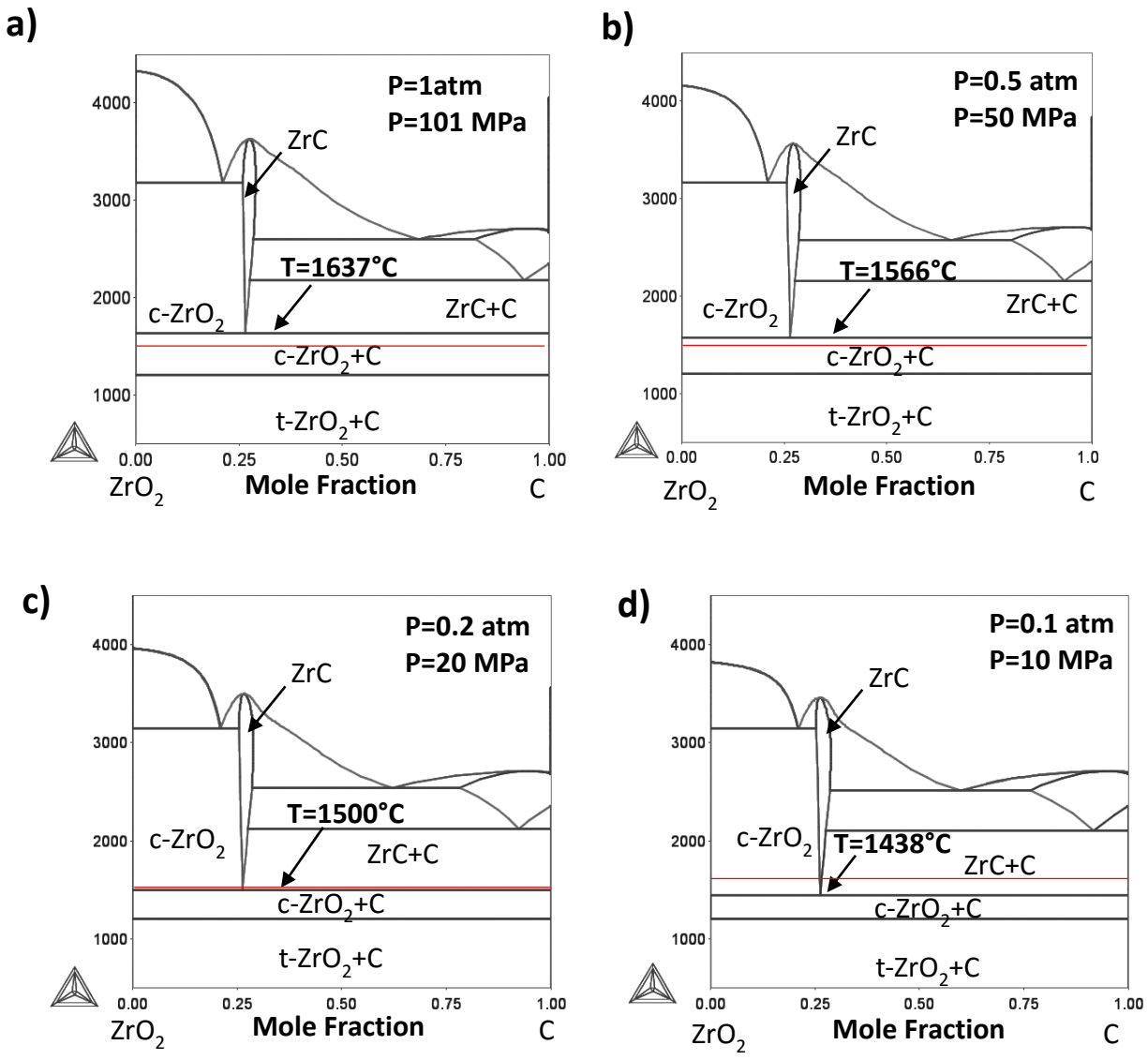

FIGURE 4.2: Pseudo-binary phase diagrams are plotted at a) 1.0 atm, b) 0.5 atm, c) 0.2 atm, and d) 0.1 atm. The red line indicates the tube furnace operating temperature. The experimental tube furnace environment must be below 0.2 atm to enable Reaction 2.

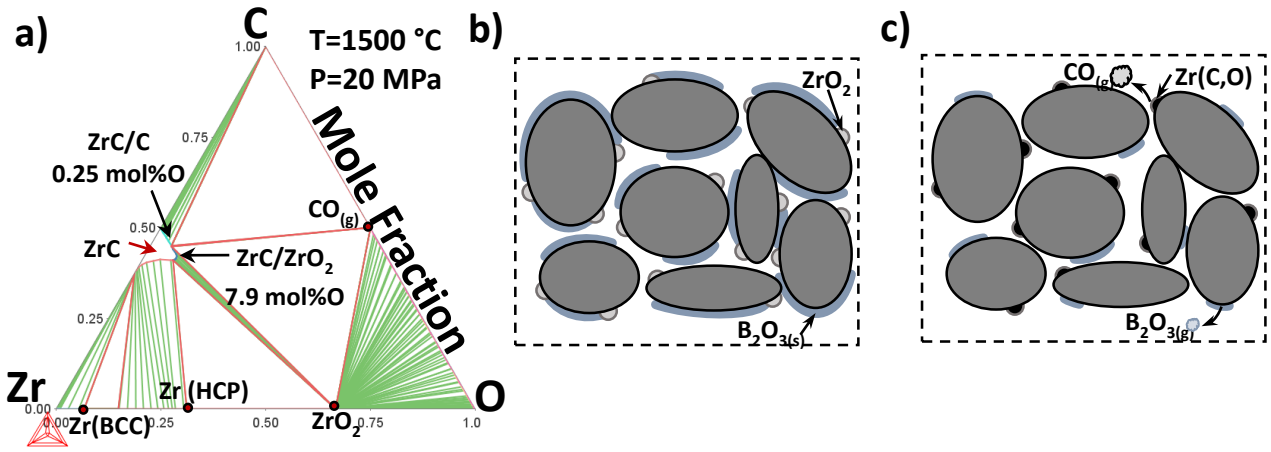

FIGURE 4.3: Preliminary ternary model of the Zr-C-O system under a) tube furnace conditions at 1500 °C and a pressure of 20MPa shows an oxygen solubility of 0.25mol% at the ZrC/C equilibrium and a maximum of 7.9 mol% oxygen solubility at the ZrC/ZrO2 equilibrium.

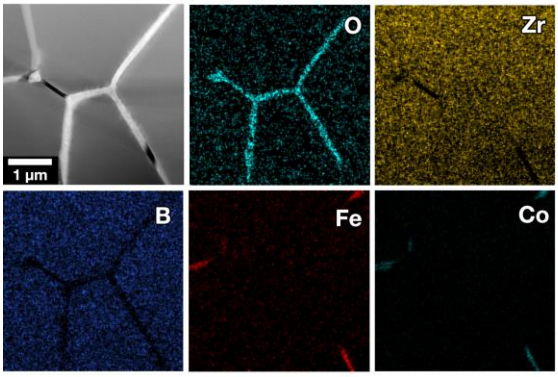

FIGURE 4.4: STEM analysis of ZrB_2+0.75C shows ZrO_2 grain boundaries that are formed from the solubility of C from ZrC_xO_y into the ZrB_2 matrix.

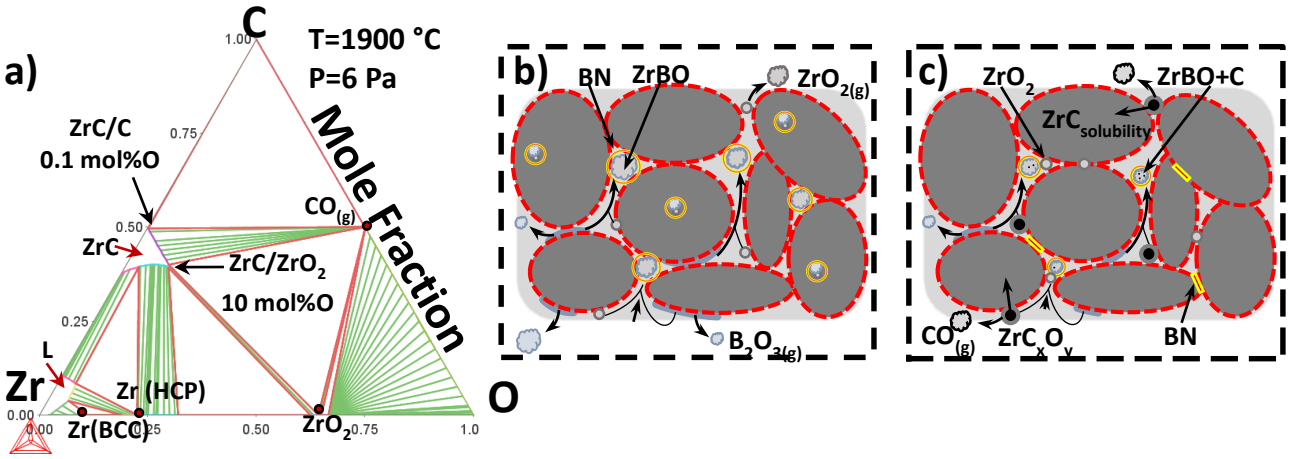

FIGURE 4.5: a) Preliminary thermodynamic model of the Zr-C-O ternary system under SPS conditions. There is minimal oxygen solubility in the ZrC/C equilibrium while there is an oxygen solubility of 10 mol% in ZrC in the ZrC/ZrO_2 equilibrium. Schematics are shown for b) BM-ZrB_2 and c) ZrB_2+0.75C. BM-ZrB_2 has a high initial oxygen content that results in oxide impurities at grain boundaries and within the grain. ZrB_2+0.75C has reduced oxygen content during SPS, but forms ZrO_2 particle impurities.

CHAPTER 5

SPS Densification of Zirconium Diboride with Boron Carbide Additions

5.1 Abstract Statement

We develop the first Zr-B-C-O quaternary thermodynamic model and use it to predict phase impurities in ZrB_2 processed with B_4C. The ZrO_2-B_4C pseudo binary and ZrB_2-ZrO_2-B_4C pseudo ternary phase equilibria shows effective oxide removal using B_4C. Surface oxides can be experimentally reduced to a minimum with B_4C additions with SPS rapid processing to produce ZrB_2 with fine grains and the highest reported room temperature strength of 660MPa. With continued work, the thermodynamic model can be expanded to include additional materials to predict microstructures for composite systems.

5.2 Abstract

A thermodynamically assisted powder processing approach is shown to produce high purity (0.06 wt%O) ZrB_2 ceramics using minimal B_4C additions (0.25wt%) and spark plasma sintering. Scanning electron microscopy and scanning transmission electron microscopy with elemental spectroscopy are used to identify unique “trash collector” oxides. These “trash collector” oxides are composed of manufacturer powder impurities that form discreet oxide particles due to the absence of the standard Zr-B-O oxides found in high oxygen samples. A preliminary Zr-B-C-O quaternary thermodynamic database developed as a part of this work was used to calculate the ZrO_2-B_4C pseudo-binary phase diagram and ZrB_2-ZrO_2-B_4C pseudo-ternary phase diagrams. We use the calculated equilibrium phase diagrams to characterize the oxide impurities and show the direct

reaction path that allows for the formation of an ultra-high purity ZrB_2 with very fine grains (3.3 μm) and superior mechanical properties (flexural strength of 660MPa).

5.3 Introduction

Zirconium diboride (ZrB_2) is an ultra-high temperature ceramic (UHTC) with attractive properties for extreme hypersonic flight environments and energy applications[29]. Owing to a combination of ionic, metallic and covalent bonding[64], ZrB_2 offers desirable properties -- low density (6.09 g/cm^3), high strengths for mechanical stability[10], and high thermal and electrical conductivities[65] -- that are attractive for advanced UHTC composites[66, 67]. However, high temperature mechanical properties of ZrB_2-based composites are highly dependent on impurity content of the matrix material, specific to the oxides, limiting application at temperature[68–70]. In response to reducing powder impurities, there is growing interest from the community to produce high purity powder sources[71] with high surface area for improved sinterability through the development of wet chemistry powder synthesis techniques[6, 8]. Unfortunately, these synthesis techniques are currently limited to small batch sizes[5, 72].

High purity processing of ZrB_2 with oxide reducing additives such as carbon or boron carbide (B_4C) is a common practice[27, 73, 74] that is scalable and can be applied to readily available manufacturer powder. In a previous study we proposed an experimental methodology assisted by equilibrium phase diagrams to process high purity ZrB_2 powders with carbon additions and proceeded to determine the thermodynamic driving forces that result in the observed microstructure using spark plasma sintering (SPS)[57]. While we found the amount of carbon required for the most effective removal of oxygen present in the sample in the form of ZrO_2 impurities, we determined that carbon as an oxide reducing

agent is not effective. Using the calculated Zr-O-C ternary phase diagram, we revealed the C-ZrO_2 reaction mechanism which leads to the formation of zirconium oxycarbide ($Zr(C_{1-x}O_x)$), under powder heat treatment conditions and subsequent development of discreet ZrO_2 particle impurities after SPS. Moreover, the ternary section revealed a $Zr(C_{1-x}O_x)$ phase with a minimum percentage of oxygen that can co-exist in equilibrium with pure carbon, thus making further oxygen removal unfeasible under the processing conditions. In this study, we focus on applying the same phase diagram-assisted experimental methodology with B_4C as an oxide reducing agent, instead of carbon, and provide a reaction path/mechanism for processing even higher purity ZrB_2 ceramics. We compare mechanical properties of as-processed ZrB_2, ZrB_2 with carbon additions and high purity ZrB_2 with B_4C.

5.4 Materials and Methods

5.4.1 Ceramic Powders

Commercially available zirconium diboride powder (grade B ZrB_2, H.C. Starck, Newton, MA) is used for this study. Oxygen content was measured using the LECO® inert gas fusion method using infrared and thermal conductivity detection. Carbon content is measured using LECO® combustion analysis and infrared detection (services provided by NSL Analytical Services, Cleveland, OH). Powder chemical and physical properties are shown in

TABLE 5.1.

5.4.2 Powder Processing Using Phenolic Resin (Carbon) and Boron Carbide

The powder processing approach was performed in several steps to 1) determine the amount of ZrO_2 on the powder surface, 2) calculate the amount of B_4C required for a stoichiometric reaction with ZrO_2, 3) determine the additive concentration with the highest thermodynamic efficiency, defined as the additive amount that results in the most oxygen removal (least measured oxygen) with the least amount of residual additive (least measured carbon), after heat treatment in a tube furnace, and 4) consolidation of high purity powder in the SPS.

As-received ZrB_2 powder was ball milled (BM-ZrB_2) using 400 g Co-bonded WC media (8 mm satellites, Union Process, Akron, OH) in 10 cm^3 batches in a 250 mL Nalgene bottle for 24 hours at 150 RPM with 125 mL of hexane (ACS Grade Hexane, BDH, Chester, PA, USA). Solvent from the milled powder suspension was rotary evaporated (IKA RV10 Digital, Wilmington, NC, USA) and sieved using a 150 μm mesh. WC media contamination was measured by weighing the media before and after milling. BM-ZrB_2 contains 0.46 vol% WC-Co media contamination and oxygen content increases to 0.94 wt%. ZrB_2 powder processed with carbon (ZrB_2+C) was prepared according to a previous study[57].

Boron carbide is added using either a large particle size B_4C powder (B_4C 99+% [reported particle size: 10.72 μm], Alfa Aesar, Ward Hill, MA, USA) or a fine particle size boron carbide powder (B_4C grade HD20 [manufacturer reported particle size: 0.9 μm], H.C. Starck, Newton, MA). B_4C is added in additions of 0.25 wt% (below stoichiometry), 0.50 wt% (stoichiometric reaction), and 0.75 wt% (above stoichiometry) with coarse B_4C

and fine B_4C, based on a powder oxygen content of 0.47wt% from ZrO_2. ZrB_2 with B_4C additions are ball milled using the same technique as above for BM-ZrB_2.

5.4.3 Powder Pre-Heat Treatment and Preparation for Chemical Analysis

ZrB_2 with each B_4C additive concentration is pre-heat treated using a tube furnace (1600 Series Horizontal Tube Furnace, CM Furnaces Inc., Bloomfiled, N.J., USA) at 1500 °C for 1 hour with flowing high purity argon at 6 cm/min to determine the efficiency for oxide removal. The tube furnace is loaded with 2 zirconia boats lined with grafoil (0.127mm thick [0.005in] Cupps Industrial Supply Inc., Tucson, AZ). The first boat is placed at the center of the furnace, which contains powder for B_2O_3 removal and ZrO_2 reduction. The second boat is filled with titanium sponge (99.95%, 3-19mm, Alfa Aesar, Ward Hill, MA, USA) to act as an oxygen getter for the flowing argon. The furnace is purged for 1 hour prior to starting the heat treatment program: heating rate of 5 °C/min to a target temperature of 1500 °C with a 1 hour dwell time, followed by cooling at 10 °C/min to room temperature. After heat treatment, oxygen and carbon content are measured. Powder samples are prepared for chemical analysis by placing them in 10mL scintillation vials and backfilling with Ar before shipping for oxygen and carbon content measurements.

5.4.4 Spark Plasma Sintering and Chemical Analysis of Dense Parts

An SPS furnace (SPS 10-3 Thermal Technologies LLC, Santa Rosa, CA) is used to densify powders. Graphite dies (Isocarb 85, Electrodes Inc., Milford, CT, USA) with a 20 mm inner diameter and 50 mm outer diameter are lined with grafoil and loaded with 4.6 g of powder to make 20 mm discs. The SPS temperature control program is set for a heating rate of 100 °C/min to 1900 °C with a 5 min dwell time, and cooling rate of 100 °C/min. After SPS, density of ZrB_2+0.25B_4C is measured using the Archimedes method with

distilled water. Relative density of parts is reported from a calculated theoretical density based on ZrB_2 as 6.09 g/cm^3 and Co-bonded WC as 14.9 g/cm^3. Oxygen and carbon content for SPS parts are measured for oxygen and carbon content. Samples for chemical analysis are pulverized to <0.2mm particulates using a steel mortar and pestle. A high-powered magnet is used to remove steel contamination from the pulverized sample before loading into a 10 mL scintillation vial, backfilling with argon and shipping for measurement.

5.4.5 SEM Characterization of Microstructure and Grain Size

Ceramics are prepared for microstructure and grain size analysis by polishing discs with a progression of polishing pads: 120 grit diamond, 220 grit diamond, 40 μm diamond, 25 μm diamond, and mirror finishing with 1200 grit silicon carbide. A field emission scanning electron microscope (S-4800 Field Emission Scanning Electron Microscope, Hitachi Inc, Pleasanton, CA) is used for microstructural analysis for grain size and impurity particle detection. SEM samples are examined using secondary electrons at 15 kV and 10 μA collected through the objective lens in the upper detector. For grain size measurements, mirror polished samples undergo wet chemical etching with molten NaOH at 500 °C for 7 seconds in a graphite crucible on a hot plate followed by a distilled water quench. SEM micrographs for grain size analysis are measured using ImageJ (ImageJ 1.44o, National Institute of Health, Bethesda, MD) imaging software reporting the maximum ferret diameter – several SEM images are used to obtain a minimum of 200 counted grains.

5.4.6 Thermodynamic Modeling for the Zr-O-C-B Quaternary System

A preliminary thermodynamic modeling of the Zr-O-C-B quaternary system is performed using the CALPHAD approach. Thermodynamic descriptions of the binaries,

Zr-O[59], Zr-C[58], Zr-B[75], C-O, C-B[76] are taken from literature. In the case of B-O binary, a preliminary thermodynamic description is obtained in this work. Due to the lack of experimental thermochemical data pertaining to the liquid phase on the B-O system, its interaction parameters were estimated based on the experimental phase diagram data (i.e. invariant temperature, congruent melting point, and the liquidus temperatures). Within the temperature range of interest (1500-1900°C), the only ternary solid solution (with significant solubility extending into the ternary composition space) is the zirconium oxycarbide, $Zr(C_{1-x}O_x)$ on the Zr-O-C ternary system and its interaction parameters were estimated based on the experimental phase diagram data available in literature[60]. A complete thermodynamic modeling of the Zr-C-O-B quaternary system obtained within the CALPHAD framework will be published elsewhere[77]. The thermodynamic and phase diagram calculations are performed using Thermo-Calc software (Thermo-Calc Software AB, version 3.0.1.1, Stockholm, Sweden).

5.4.7 STEM Specimen Preparation, Characterization and Analysis

ZrB_2+0.25B_4C sintered discs are prepared into machined coupons (1.5 mm x 2.0 mm x 0.5 mm) for STEM specimen preparation. The coupons are then mechanically polished to electron transparency using an Allied Multiprep^{TM} and further thinned using a Fischione 1050 argon ion mill operated using energies between 200 eV and 2 keV while maintaining LN_2 cooling.

Specimens are examined using a probe-corrected FEI Titan G2 60-300 kV TEM/STEM operated at 2000 kV and equipped with a high brightness X-FEG electron source, a Super-X detector for energy dispersive X-ray spectroscopy (EDS), and Gatan Enfinium spectrometer for electron energy loss spectroscopy (EELS). Data acquisition and

post processing of the EDS data is performed using Bruker Espirit software. The characteristic K lines are used for mapping every element. Twenty high angle annular dark-field (HAADF) images covering an approximate area of 100 μm^2 were acquired to provide a large sampling size for microstructural characterization. For confirmation of the phase identity in each region, electron energy loss spectroscopy (EELS) is acquired and processed using Gatan Digital Micrograph.

5.4.8 Toughness By Indentation and Flexural Strength

Mechanical propertieqs for ZrB_2+0.25B_4C are compared to BM-ZrB_2 and ZrB_2+C samples produced in previous work using the same SPS sintering conditions[57]. Vicker's microhardness is performed using a microhardness testing system (DV6013, Buehler LTD, Lake Bluff, Illinois, USA) using a load of 0.3 kgf at a loading rate of 100 μm/sec and load time of 20sec on mirror polished samples.

Toughness is measured and calculated using the direct crack measurement method via the Anstis method[78] on mirror polished samples. A microhardness testing system is used to apply a load of 0.5 kgf to encourage crack formation during indentation at a loading rate of 100 μm/sec and load time of 20sec.

Flexural strength testing is performed using a 4-point bend test setup with a semi-articulating fixture with a load span of 14 mm attached to an Instron 5965 (Instron, Norwood, MA, USA) and tested according to ASTM Standard C1161. Bars are machined from 20 mm discs to modified A-bars (1.5 mm x 2.0 mm x >15 mm) using a precision surface grinding machine (Model 618/620 AD, Jet Tools North America, La Vergne, TN,

USA). Flexure strength bars are imaged after testing for fracture surface analysis under SEM.

5.5 Results and Discussion

5.5.1 Oxygen Content and SPS Densification Of ZrB_2+B_4C

ZrB_2 with the additions of fine B_4C have higher thermodynamic efficiencies for oxide removal in the tube furnace. Minimum oxygen and carbon content are measured for 0.25 wt%B_4C (fine) additions, herein referred to as ZrB_2+0.25B_4C. Therefore, ZrB_2+0.25B_4C is chosen for densification of high purity ZrB_2 ceramics using SPS. Chemical and physical properties of ZrB_2 with B_4C additions can be found in

TABLE 5.1.

TABLE 5.1: Summary of properties for ZrB_2 and processed ZrB_2 with C and B_4C additions

Powder System	Additive Particle Size (μm)	Additive Amount (wt%)	Oxygen Content (wt%)	Carbon Content (wt%)
As received ZrB_2	-	0	0.84	0.08
Ball milled ZrB_2	-	0	0.97	0.27
Heat Treated ZrB_2+B_4C	10.7	0.75	0.34	0.17
Heat Treated ZrB_2+B_4C	10.7	0.50	0.32	0.10
Heat Treated ZrB_2+B_4C	10.7	0.25	0.35	0.05
Heat Treated ZrB_2+B_4C	0.9	0.75	0.25	0.08
Heat Treated ZrB_2+B_4C	0.9	0.25	0.25	0.01

SPS is an efficient means of densifying ZrB_2 due to joule heating of the sample and die, which promotes rapid sintering times and control of the microstructure. The shrinkage profile for ZrB_2+0.25B_4C has a delayed onset of densification with rapid densification starting near 1550 °C in comparison to BM-ZrB_2, shown in **FIGURE 5.1**. The delayed onset of densification is attributed to the lack of oxides found on the particle surface that would otherwise promote particle rearrangement through vapor phase transport and encourage grain growth. After SPS, ZrB_2+0.25B_4C has a reduced oxygen contamination of 0.06 wt% O with an average grain size of 3μm.

Therefore, the thermodynamic processing conditions used to purify ZrB_2 with powder heat treatments and the additions of fine B_4C are shown to be effective at evolving B_2O_3 and reacting with ZrO_2 to prevent grain coarsening, as depicted in **FIGURE 5.2b**. SPS of ZrB_2+0.25B_4C further reduces oxygen contamination to a minimum, **FIGURE 5.2c**. The ability for SPS to further reduce oxygen contamination due to the application of current is well noted in literature with various proposed cleaning mechanisms[47, 49]. Future work on the effect of sample current density on oxide removal on high purity ZrB_2+0.25B_4C is on-going.

5.5.2 Microstructure Analysis Using SEM and STEM

After SPS, microstructural analysis on ZrB_2+0.25B_4C confirms the minimal measured oxygen contamination; however, there is evidence of BN platelets pinned at grain boundaries, shown in **FIGURE 5.3b**. BN platelets have been seen in a previous study[57] where they begin to appear in abundance when cleaning techniques are performed on the powder. The origin of the BN is predicted to come from the N-impurities in the source

powder. It has also been suggested that N-impurities develop due to the ball milling environment when jars are not backfilled with an inert atmosphere[79].

Oxide impurities and grain boundaries are then analyzed by STEM to determine how B_4C affects the chemistry. The STEM micrograph, presented in **FIGURE 5.3c**, shows oxide phases scattered throughout the microstructure and lamellar BN pinned between grain boundaries. EDS analysis of these oxides (**FIGURE S5.1**) shows an oxide chemistry that contains low amounts of amorphous Zr-B-O in comparison to ZrB_2+C[57]. From bulk chemical analysis, oxygen content is reduced to 0.06 wt% O, which is lower than that found in literature where B_4C additions are used to enhance powder purity[23, 80]. A thermodynamic model is developed in order to understand the enhanced cleaning effects with B_4C.

5.5.3 Thermodynamic Evaulation on the Reducing Effects of Boron Carbide on Oxygen

In order to remove ZrO_2 contamination from the powder surface using boron carbide, the following idealized thermodynamic reaction is proposed:

$$7ZrO_2 + 5B_4C \rightarrow 7ZrB_2 + 3B_2O_{3(l)} + 5CO_{(g)} \qquad (1)$$

FIGURE 5.2a shows the calculated ZrO_2-B_4C pseudo-binary phase diagram from the preliminary Zr-O-C-B quaternary database developed in this work. More specifically, under the tube furnace and SPS processing temperatures (1500 to 1900 °C), the equilibrium phase diagram shows three distinct phase regions depending on the relative proportions of ZrO_2 and B_4C: 1) ZrO_2, ZrB_2, liquid oxide, and gas when a smaller percentage of B_4C relative to the ZrO_2 is used (<42mol% B_4C), 2) ZrB_2, liquid oxide, and gas when close to the exact fraction of B_4C addition (as given in equation 1) is used, and 3) a region with

ZrB_2, B_4C, liquid oxide, and gas when excess B_4C is used (>42mol% B_4C). The liquid oxide is composed of a mixture of ZrO_2 and B_2O_3 as shown in the ZrO_2-B_2O_3 binary[62] and the gas composition is composed of CO and $B_2O_{3(g)}$. Regardless of the amount of B_4C additions used, it is evident that the reduction reaction leads to the formation of ZrB_2 and B_2O_3 liquid as proposed in Reaction 1. Above 2100°C around 0.45 mol%B_4C, the phase diagram predicts a region of phase pure ZrB_2 in equilibrium with gas. Although we can experimentally achieve the high temperatures in SPS to obtain pure ZrB_2 and evolve gas, undesirable grain growth will result during processing. Furthermore, during powder heat treatment with flowing Ar and SPS under high vacuum (6Pa), $B_2O_{3(l)}$ evolves as $B_2O_{3(g)}$, due to its high vapor pressure[21, 23], we can obtain the same oxide removal at lower temperatures.

Further, a pseudo-ternary of ZrB_2-ZrO_2-B_4C is calculated in order to examine a possible reaction path during SPS (**FIGURE 5.3a)**. The ternary diagram is calculated by suspending any gas interactions which would be evacuated during SPS, as such, C is present in the phase diagram where it would ordinarily be defined by $CO_{(g)}$. The ternary clearly shows the reaction path for ZrO_2+B_4C to efficiently react and form ZrB_2, in comparison to carbon that forms products with oxygen solubility[57]. Experimentally, the efficiency of B_4C to remove oxygen is highly dependent on the reaction diffusion paths, which is a function of additive particle size[81]. Due to the reaction efficiency being governed by the diffusion path and direct contact between B_4C particles and oxides, the maximum potential to reduce ZrO_2 is not reached when stoichiometric or coarse B_4C additions are used (

Table 5.1) - rather there is an incomplete reaction and excess B_4C is detected in the powder. By using sub-stoichiometric B_4C additions, the reaction comes to completion, leaving minor oxides on the powder surface that are removed through SPS oxide cleaning capabilities to produce an oxide free microstructure with minimal impurities.

5.5.4 Chemical Analysis of Grain Boundary and Interparticle Impurities

Spectroscopic investigation of ZrB_2+B_4C particle impurities shows two distinct impurity compositions. **FIGURE 5.4a** shows an oxide impurity composed of amorphous Zr-B-O-Ca surrounded by a lamellar BN structure. Within the oxide, EDS identifies particles with large concentrations of C. Close inspection using EELS (**FIGURE 5.4b**) at 4 points along the oxide identifies a Zr[82] and B[83] matrix profile at Point 1, a BN[84] spectra for Point 2. Point 3 shows a region containing Zr, B, amorphous C, Ca, and O[85]. Point 4 verifies carbon in the oxide with a fine edge structure characteristic of diamond sp^3 bonding rather than unreacted B_4C. A study using HfB_2 processed with B_4C also shows the presence of nanocrystalline carbon, where the carbon source is postulated to come from having either a sub-stoichiometric carbon rich boron carbide ($B_{4-x}C$) or dissolution of C from HfB_2-WC forming $(Hf,W)B_2$ and precipitating C[79]. Due to the low WC contamination in our ball milled powder, the carbon source is believed to come from our carbon-rich B_4C (manufacturer boron:carbon ratio reported as $B_{3.8}C$). The presence of carbon in the oxide is also supported in the binary phase diagram (**FIGURE 5.2a**), at SPS sintering temperatures.

FIGURE 5.4c shows an oxide impurity with a highly complex chemistry including an abundance of different manufacturer powder impurities. This “trash collector” effect is suspected to form due to the minimization of ZrO_2 and B_2O_3 in the microstructure that forces the impurities to dissociate from the powder and localize in discreet impurities. BN

impurities (**FIGURE 5.4d**) pinned between grain boundaries also appear to accumulate oxygen from the surroundings and prevents congregation at the grain boundaries. The grain boundary chemistry is composed of low melting metal impurities of Fe and Co, where Fe is derived from manufacturer powder impurities and Co comes from the milling media. The absence of oxygen at the grain boundaries allows ZrB_2+0.25B_4C to densify with minimal oxide grain growth effects, resulting in a fine grained microstructure.

5.5.5 Mechanical Properties of ZrB_2 Processed with Carbon and B_4C

Vicker's microhardness (VH), flexural strength and toughness measurements via the Anstis Method[78] are provided in **TABLE 5.2** for BM-ZrB_2, ZrB_2+C and ZrB_2+0.25B_4C. BM-ZrB_2 has the lowest material properties due to the high oxygen content (B_2O_3 and ZrO_2) that encouraged grain coarsening. The presence of oxides softened the material which resulted in a low hardness (VH 11.5GPa) and the large grains limited flexural strength to only ~430MPa. ZrB_2+C with a lower oxygen content exhibits an increase in hardness (VH 14.9GPa), however flexural strength did not improve due to this material still having a large grain size. ZrB_2+0.25B_4C is the most effective at significantly reducing oxygen content, which resulted in the smallest grained pure ZrB_2 with the highest flexural strengths reported in literature of 660 GPa and seems to have surpassed strengths predicted by the Griffith relationship as proposed by Thompson et. al[16].

TABLE 5.2: Summary of chemical and mechanical properties for ZrB_2 processed with C and B_4C additions

Powder System	Powder Oxygen Content	Oxygen Content After SPS	Relative Density	Density (g/cc)	Avg Grain Size (μ m)	Avg Hardness (GPa)	Toughness ($MPa \cdot m^{½}$)	Flexural Strength (MPa)
BM-ZrB_2	0.94	0.18	99.6%	6.12	9.0	11.5	2.3±0.4	428± 59
ZrB_2+C	0.47	0.12	100.2%	6.15	8.2	14.9	2.0±0.1	417 ± 66

ZrB_2+ $0.25B_4C$	0.25	0.06	99.3%	6.07	3.3	14.4	3.2±0.2	660 ± 68

BM-ZrB_2 fracture surfaces (**FIGURE 5.5a**) show dominant transgranular fracture. The low fracture toughness (2.3 MPa·$m^{½}$) was expected to arise from the high oxide contamination, however, an interaction of the oxide impurity phases and the fracture is not obvious. ZrB_2+C (**FIGURE 5.5b**) shows a mixture of transgranular and intergranular fracture. The change in the fracture mode for ZrB_2+C seems to be driven by the carbon impurities that are easily noticed in the fracture surface and may also be caused by the discreet ZrO_2 impurity particles detected in previous work[57]. The interaction with impurities has thus decreased the toughness of the material (2.0 MPa·$m^{½}$) in comparison to BM-ZrB_2, despite the slightly lower grain size and oxygen content. The fracture surface of ZrB_2+0.25B_4C (**FIGURE 5.5c**) has a high degree of transgranular fracture, and is similar to that noted in literature[13, 86]. The higher toughness (3.2 MPa·$m^{½}$) for ZrB_2+0.25B_4C is expected to arise from the higher purity microstructure. Future work is on-going for investigation of high temperature mechanical properties of ZrB_2+0.25B_4C.

5.6 Summary and Conclusion

A thermodynamically driven powder processing methodology is applied to ZrB_2 using B_4C as an oxide reducing agent to produce an ultra-low oxide impurity specimen. The use of a thermodynamic model of the Zr-B-C-O quaternary is used to develop phase diagrams that shows evidence of a direct reaction path to reduce ZrO_2, resulting in low powder oxygen content after powder pre-heat treatment (0.25 wt%O) and subsequent densification in SPS (0.06 wt%O) to produce a very fine grained (3.3 μm) and high purity

microstructure. Due to the low Zr-B-O oxide content, unique oxide impurities are formed in ZrB_2+0.25B_4C. These “trash collector” oxides are instead predominantly comprised of manufacturer powder impurities of Ca, Fe, Y, Al, and Ag. Mechanical properties are measured for BM-ZrB_2, ZrB_2+C and ZrB_2+0.25B_4C. ZrB_2+0.25B_4C has superior mechanical properties to other processing methods (flexure strength of 660MPa, toughness of 3.2 MPa·$m^{½}$) due to the high purity processing methodology.

5.7 Acknowledgements

A National Science Foundation Early Faculty Career Award under Division of Materials Research-0954110 supports material processing of ceramics using spark plasma sintering. J.H.D. acknowledges support for this work by the National Science Foundation Graduate Research Fellowship (Grant DGE-1252376). The authors acknowledge the use of the Analytical Instrumentation Facility (AIF) at North Carolina State University, which is supported by the State of North Carolina and the National Science Foundation.

5.8 Figures

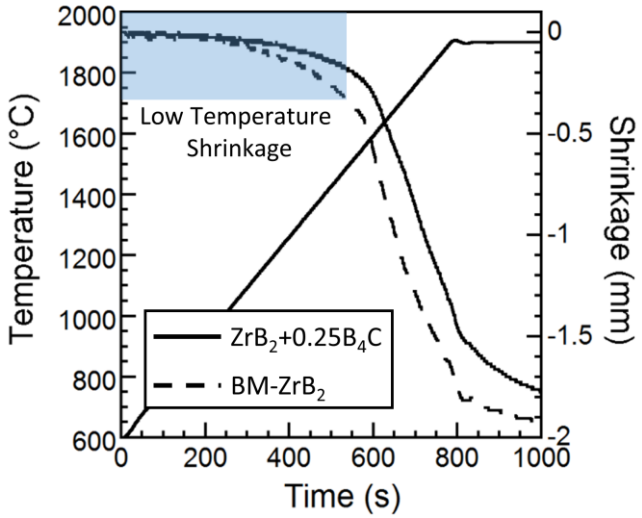

FIGURE 5.1: Densification profile for ZrB_2+0.25B_4C and BM-ZrB_2. ZrB_2+0.25B_4C has lower oxygen content and does not exhibit low temperature shrinkage attributed to vapor phase oxides that promote grain growth.

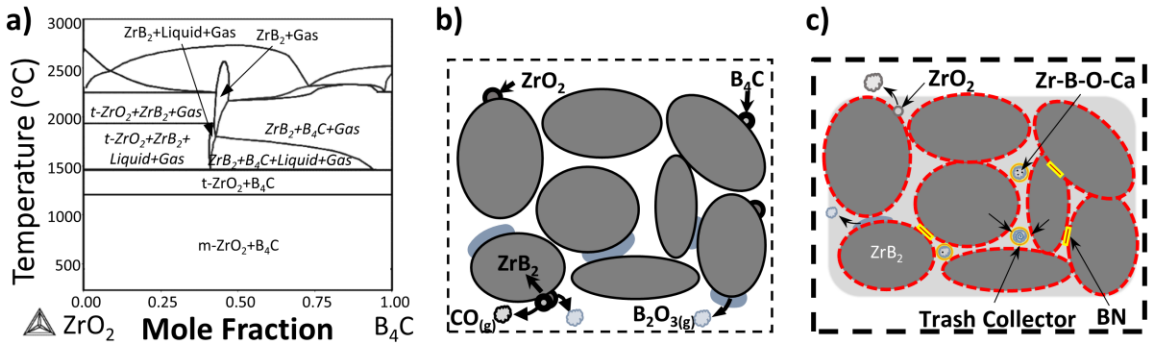

FIGURE 5.2: a) Preliminary Thermo-Calc pseudo-binary phase diagram of the ZrO_2-B_4C system. b) ZrB_2+0.25B_4C is heat treated in the tube furnace to evolve $B_2O_{3(g)}$ and allows ZrO_2 to react into ZrB_2 and $B_2O_{3(g)}$ to minimize oxide contamination bfore SPS. c) SPS reduces oxygen urther with applied current and to develop unique "trash collector" oxides made of manufacturer powder impurities.

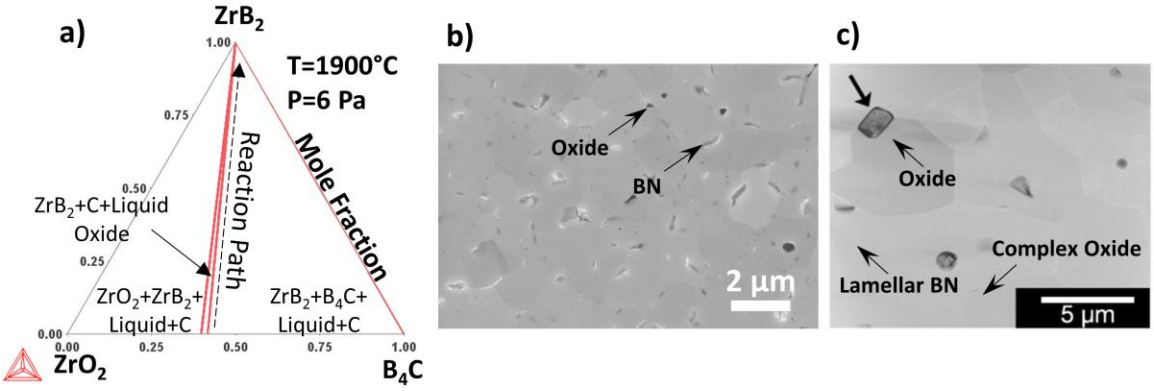

FIGURE 5.3: a) Preliminary quaternary phase diagram of ZrB_2-B_4C-ZrO_2 is presented under SPS sintering conditions of T=1900°C and P=6Pa that shows a direct reaction path for oxygen reduction to form high purity microstructures as shown in c) SEM and d) STEM.

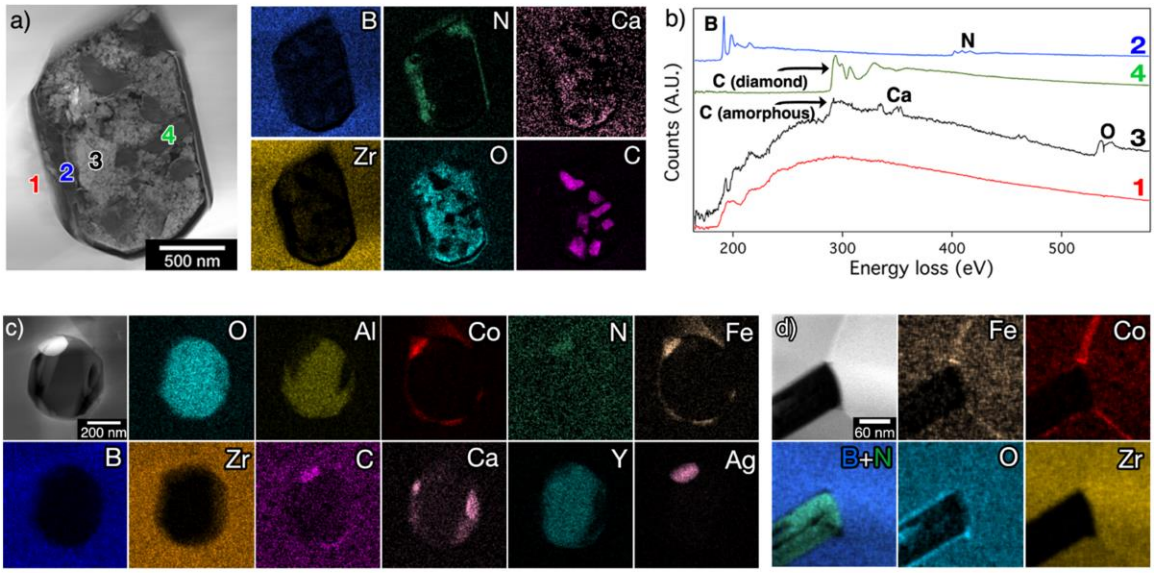

FIGURE 5.4: a) Oxide compositions are detected using STEM EDS to show minimal Zr-B-O oxide contamination. b) EELS analysis verifies the Zr-B-O oxide with Ca and carbon contamination, possibly in the form of diamond. c) Additional oxides are found that act as "trash collectors" for manufacturer powder impurities, and d) BN phases are also shown to draw in oxygen contamination, leaving the grain boundaries with Fe-Co.

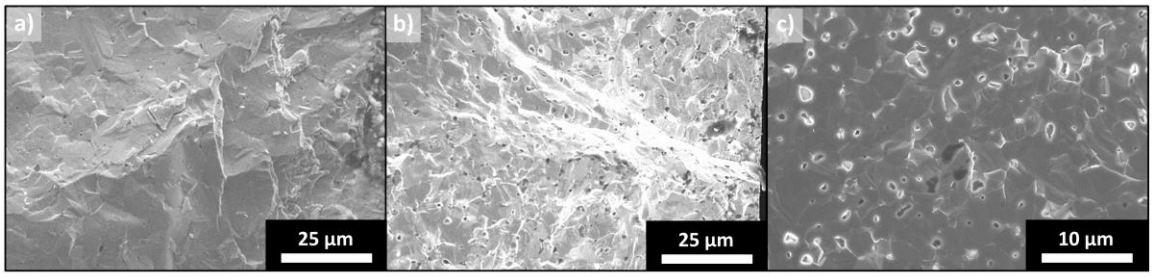

FIGURE 5.5: Fracture surfaces from flexural bar testing shows a change of fracture mechanics when reducing agents are added. a) As-milled ZrB_2 has a dominant intergranular fracture mode with sharp planar edges and when b) carbon additions are used, becomes a mixture of transgranular and intergranular with the appearance of rounded edges. Fracture surfaces for c) B_4C additions are on a smaller scale and show mostly transgranular fracture.

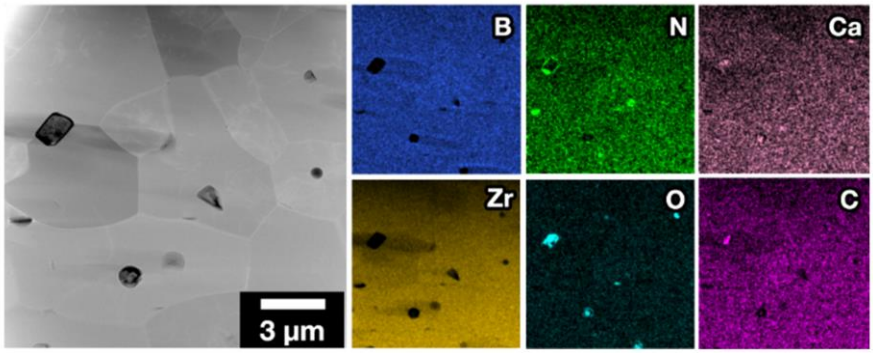

FIGURE S5.1: STEM EDS maps for ZrB_2+0.25B_4C shows oxide impurities with chemistries that lack the traditional Zr-B-O amorphous oxide.

CHAPTER 6

SCALE UP PROCESSING USING FINITE ELEMENT ANALYSIS MODELING OF SPS

6.1 Abstract Statement

A model is developed to show thermal gradients and current density maps for the spark plasma sintering system using an electrical conductor and electrical insulator. The model couples thermal and current effects to include contact resistances and calibrated to 20mm disc tooling. ZrB_2 and Si_3N_4 are processed in the SPS and microstructurally characterized for scale-up procedures. The model is used and shows the first successful scale-up of ceramics that require processing at high temperature, up to 1900°C, to a 30mm disc through current density manipulation. The model is used to predict tooling needed to produce uniform 100mm discs.

6.2 Abstract

Current-assisted sintering techniques like spark plasma sintering are highly dependent on tooling resistances and the electrical conductivity of the sample, which influences the part uniformity through localized heating spots that are strongly dependent on the current flow path. We use a coupled thermal-electrical finite element analysis model to investigate the development and effects of tooling and current density manipulation on an electrical conductor, zirconium diboride (ZrB_2), and an electrical insulator, silicon nitride (Si_3N_4), at the steady-state where material properties, temperature gradients and current/voltage input are constant. A model is built based on experimentally measured temperature gradients in the tooling for 20 mm discs and validate the model by producing

30 mm discs with similar temperature gradients and grain size uniformity across the part. We predict the uniform scalability of 100 mm ZrB_2 by using a hollow punch design and Si_3N_4 using a T-punch design to localize current density and joule heating around the sample cold regions.

6.3 Introduction

Low-field direct current sintering techniques, such as spark plasma sintering (SPS), are gaining wide attraction for the densification of various materials due their ability to rapidly consolidate materials in minutes through the simultaneous application of pressure and direct current as opposed to conventional radiative heating methods which can take hours[28, 87–89]. Of specific interest is the ability to process nanomaterials[90] and non-equilibrium phases in metals and ceramics[34, 35] with enhanced mechanical properties[45, 61] by taking advantage of SPS-unique phenomena such as dielectric breakdown of oxides[40], electromigration[48, 91], and localized interparticle heating[52] to control densification and grain growth kinetics.

Due to the desirable properties produced in lab-scale specimens[92–94], there is a need to reproduce these results at a larger scale and to near-net shape and complex geometries. During scale-up processing to form dense samples, sintering temperature and pressure from lab-scale specimens are used with an increase in densification dwell time. Although this produces dense samples, microstructural non-uniformities exist due to non-uniform sample temperature gradients. SPS is highly dependent on the system tooling resistance, which increases the difficulty in producing large scale parts with comparable homogeneous microstructural properties, due to thermal and stress gradients[95] that results from current flow paths.

In the present work, we investigate two case studies using a thermal-electrical coupled model in SPS using two sample materials, (1) an electrical conductor (zirconium diboride [ZrB_2]) and (2) an electrical insulator (silicon nitride [Si_3N_4]), to explain the influence of sample electrical conductivity, tooling resistance and tooling geometry on the current flow path and sample temperature gradient. The model is developed using a 2-D axis symmetric representation of the tooling focused on the sintering dwell time, or steady-state, where experimental current and voltage are constant, sample temperatures are at a maximum, and material properties do not change. The model is calibrated for a 20 mm disc and subsequently used to predict tooling and SPS conditions to produce uniform 30 mm discs. With empirical evidence of the model accuracy, we can predict the tooling needed for uniform 100 mm discs of ZrB_2 and Si_3N_4.

6.4 Experimental Procedures

6.4.1 Ceramic Powders and SPS Assembly Materials

Zirconium diboride (ZrB_2, Grade B H.C. Starck, Newton, MA, USA) and silicon nitride (Si_3N_4, 5 wt% Al_2O_3, 5 wt% Y_2O_3, 1 wt% MgO, StarCeram® N Ready to Press-Grade M, H.C. Starck, Newton, MA, USA) powders are used to densify electrical conductors and insulators, respectively\. For this study, powders are used as-received without additional powder processing. **FIGURE 6.1** shows a schematic of the SPS assembly centered on the specimen within the conductive graphite tooling. This assembly includes two electrodes made from 321 stainless steel. The die, punches, spacers, and hot/cold rams are made from graphite (Isocarb 85, Electrodes, Inc., Milford, CT, USA) with tooling dimensions listed in **TABLE 6.1**. Grafoil (0.127 mm thick [0.005 in] Cupps Industrial Supply Inc., Tucson, AZ, USA) is used to line the inner die wall and powder

compact/punch interface to reduce sample/tooling reactivity during densification. Boron nitride spray (BN, Aerosol Refractory Paint, Alfa Aesar,Ward Hill, MA, USA) is applied and polished smooth with standard letter paper to provide a thin layer of electrical insulation within the die assembly for current path manipulation.

6.4.2 Spark Plasma Sintering of Zirconium Diboride and Silicon Nitride

Ceramic discs of ZrB_2 and Si_3N_4 are produced in 20 mm and 30 mm diameters and 3mm thick using an SPS furnace (SPS 10-3, Thermal Technologies Inc., Santa Rosa, CA, USA). The SPS furnace has a current capacity of 3000 A at a maximum of 10 V with a 10 ton hydraulic press working on a pulsed current setting of 25ms ON and 5ms OFF. The sintering temperature is monitored by a single-color optical pyrometer (Marathon MM1MH, Raytek, Santa Cruz, CA, USA) sighted on a small hole 2.5mm in diameter and 7.5mm into the die for 20 mm assemblies and aimed directly on the die wall for 30 mm assemblies. The temperature ramp rate and dwell time are controlled through a proportional-integral-derivative (PID) controller which moderates the current output.

Grafoil lined assemblies are loaded with powder, settled with a vibratory plate and pre-loaded using a standard press at 50 MPa for 1 min. 30 mm assemblies can include two additional graphite spacers inserted between the specimen and punch. Spacers used for Si_3N_4 are coated with boron nitride. The outer die wall is wrapped with thermally insulating graphite felt (~15 mm thickness, J.C.Cole & Associates, Inc., Epping, NH, USA) and a 12 mm hole is punched out of the center for pyrometer sighting. The packed die is loaded into the SPS furnace under a 5 MPa preload and heated to 600 °C using 767 A for 20 mm dies (893A for 30 mm dies) before ramping to target sintering temperature.

Sintering temperatures are based on densification studies to produce dense parts with minimal hold time.

TABLE 6.1: SPS tooling dimensions for 20mm and 30mm assemblies.

Component Number	SPS Component	Dimension	Value (mm)
1	Electrodes	Height Radius	26 31.75
2	Cold Ram	Height Radius	52 45
3	Hot Ram	Height Radius	22 20
4	Punch (20mm disc)	Height Radius	30 10
5	Die (20mm disc)	Height Radius	40 25
6	Sample	Height	3
7	Grafoil	Thickness	0.13
8	Die (30mm disc)	Height Radius	50 15
9	Punch (30mm disc)	Height Radius	40 15
10	Spacer (30mm disc)	Height Radius	6 15

ZrB_2 powders are loaded to 35 MPa at 30 MPa/min until the final sintering temperature is reached and released at 30 MPa/min after the 5-minute dwell time. The specimens are heated at 100 °C/min to 1900 °C, then held for 5 minutes, and cooled at 100°C/min to 1000°C, followed by natural cooling, achieved by turning off the SPS furnace power. Si_3N_4 powders are loaded to 30 MPa at 25 MPa/min to a final sintering temperature of 1700 °C and released at 25 MPa/min after the 2 minute dwell time. ZrB_2 is densified under vacuum (6 Pa) and Si_3N_4 under high purity N_2 gas.

6.4.3 Model Framework

The computational model was developed using a finite element analysis (FEA) software (COMSOL™ Multiphysics 5.0, Los Angeles, CA, USA) that allows the coupling

of joule heating and heat transfer effects to calculate current density and temperature distributions within the SPS assembly. Due to the symmetric nature of the tooling and efficiency of computation, a 2D axisymmetric model is used to represent the SPS assembly (**FIGURE 6.1**). A 3D interpretation of the current model has been produced and model results vary by <1%; however, that model will be detailed in future work focusing on complex shape modeling.

The SPS tooling geometry is built and each component is assigned a bulk material property as a function of temperature (**Appendix 6.9**). The tooling exterior surface and graphite felt are given a surface emissivity defined by the "Diffuse Surface" boundary condition. Grafoil/tooling interfaces are given an electrical contact resistance through the "Contact Impedance" boundary condition and grafoil thermal conductivity is defined using a "Thin Layer" thermal resistance boundary layer. Electrode cooling channels are defined by applying an equivalent heat transfer coefficient to the top and bottom surfaces of the electrodes. The SPS assembly is meshed using a physics-controlled mesh that decreases the element size with decreasing part size (i.e. the element mesh on the sample is much finer than the mesh used to describe the cold ram). Finally, current density (A/cm^2) or voltage (V) inputs are added to the bottom surface of the lower electrode, based on experimental values obtained from the dwell period (**FIGURE 6.2**) to generate temperature and current density distributions within the tooling. From our experience, the model for electrical insulators (Si_3N_4) only solves with a voltage input, however, the resolved current density is the same as experimental values.

6.4.4 Bulk Material Property Inputs to Model

Electrical resistivity and thermal conductivity values for graphite, Si_3N_4, ZrB_2, and steel as functions of temperature are input into the finite element model. Normalized graphite electrical resistivity and thermal conductivity reported by Mersen (Mersen USA, Bay City, MI, USA) are used in conjunction with room temperature values to describe resistivity and conductivity as functions of temperature, reported by Electrodes. Electrical resistivity and thermal conductivity as a function of temperature for the electrodes[96], ZrB_2[97], and Si_3N_4[98] are obtained from literature.

6.4.5 Interfacial and Surface Material Property Inputs

Grafoil contact resistance is determined experimentally as a function of pressure. Multiple experiments are run where the number of foil layers between experiments increases. Constant current is applied and voltage is measured as a function of increasing load from 1 MPa to 15 MPa at a rate of 1 MPa/min. Contact impedance is calculated and averaged from the change in resistance using multiple foils. Above 6 MPa the contact impedance approaches a constant value of 1.128×10^{-7} $\Omega \cdot m^2$, which is used for all high pressure interfaces where grafoil is present. Due to the differences in how voltage and current are measured per SPS system (e.g. FCT, Sumitomo), it is recommended that these contact resistance values be measured, rather than using the electrical contact resistance value above. Graphite felt is represented in the model by assigning an equivalent surface emissivity to the die wall. The graphite felt value is calibrated based on the experimentally measured temperatures of the die wall and sample temperature, resulting in an equivalent emissivity of $\varepsilon=0.076$. The SPS cooling channels are simplified through the use of a convective heat flux boundary layer with a heat transfer coefficient of 2250 (W/m·K),

estimated from the cooling capacity of the chiller (Orion Inveter Chiller RKE1500B, Liberty Hill, TX, USA) and approximate cooling channel dimensions.

6.4.6 Direct Sample Temperature Measurements

Direct sample temperature is measured using previously densified 20 mm ZrB_2 and Si_3N_4 discs in order to verify the accuracy of the model. The 20 mm tooling assembly is used for direct sample temperature measurement with modifications to the die and graphite felt. The die has an additional 2.5mm diameter hole drilled through the die and the graphite felt has a 12mm hole punched out in the same location. A secondary optical pyrometer (Raytek, Marathon MR, Berlin, Germany) is sighted at the hole and measures the sample edge temperature. Three temperatures are measured for model and experimental comparisons at "Pyrometer A" for the die wall temperature, "Pyrometer B" for the sample edge temperature, and "Thermocouple," measured using a Type K thermocouple located 3.5mm below the top surface of the bottom electrode, refer to **FIGURE 6.1**.

6.4.7 Material Characterization

After SPS, density of sintered ceramics are determined by Archimedes method where theoretical densities are 3.20 g/cm^3 and 6.09 g/cm^3 for Si_3N_4 and ZrB_2, respectively. Specimens are prepared for microstructure and grain size analysis by polishing whole discs. ZrB_2 is prepared for imaging using polishing pads in decreasing diamond grit of 120 and 220, followed by using diamond-polishing pads of 40 μm and 25 μm. The final mirror finish is achieved using a 1200 grit silicon carbide pad. For grain size measurements on ZrB_2, mirror polished samples are thermally etched in a tube furnace (Astro A247, Thermal Technologies LC, Santa Rosa, CA, USA) with flowing high purity Ar at 500 °C for 1 hour. The furnace was purged for 30 min with flowing HP argon at a flow rate of 6 cm/min at

room temperature before loading the heat treatment program. The tube furnace temperature profile increases at a rate of 5° C/min up to 500 °C and held for 1 hour before cooling at a rate of 10 °C/min to room temperature. Si_3N_4 ceramics are polished using 80, 120, 240, 400, 600 grit SiC pads, followed by mirror polishing using 1200 grit SiC. Si_3N_4 ceramics are etched using phosphoric acid (H_3PO_4, 85% aqueous solution, Alfa Aesar, Ward Hill, MA, USA) at 300 °C for 20 minutes. A field emission scanning electron microscope (S-4800 Field Emission Scanning Electron Microscope, Hitachi Inc, Pleasanton, CA, USA) is used for microstructural analysis, including grain size and microstructure uniformity across the disc diameter. SEM images are acquired using secondary electrons. ZrB_2 samples are examined at 15 kV and 10 μA using the upper detector and Si_3N_4 is plasma coated with platinum (Hummer 6.0 Sputter System, Anatech USA, Union City, CA, USA) for 40 seconds and examined at 5-10 kV and 10 μA.

SEM micrographs for grain size analysis are measured using Image J (Image J 1.6.0_20, National Institute of Health, Bethesda, MD, USA) imaging software reporting the maximum ferret diameter – several SEM images are used to obtain a minimum of 200 counted grains per condition. β-Si_3N_4 content analysis[99] is used to determine quantitative phase content across the diameter of 20 and 30 mm discs using X-Ray diffractometry (Phillips X'Pert MPD, Westborough, MA, USA) on 5 mm x 5 mm sections of each disc. A Cu K-alpha radiation source is used with 2° slit size, and scan range 25-30°. Peak height ratio (PH) is measured by dividing α(200) peak intensity, located at approximately 26.5°, by β(200) peak intensity, located at approximately 26.9° according to Pigeon et. al[99]. Weight fraction of α is calculated by: $(\alpha/\beta) / (1 + \alpha/\beta)$.

6.5 Results and Discussion

6.5.1 Fundamentals of SPS: Electrical and Thermally Coupled Physics

The applied electric current during SPS results in joule heating and subsequent heat transfer as governed by the steady state equation (Equation 1):

$$\rho C_p \mathbf{u} \cdot \nabla T = \nabla \cdot (k_T \nabla T) + Q_e \quad (1)$$

$$Q_e = \boldsymbol{J} \cdot \boldsymbol{E} \quad (2)$$

where ρ is density, C_p is the specific heat capacity, $\boldsymbol{u}$ is a fluid velocity where convection is present, but is generally negligible, T is temperature, k_T is thermal conductivity, and Q_e is heat generated per unit volume, defined in Equation 2, where $\boldsymbol{J}$ is the current density and $\boldsymbol{E}$ is electric field.

The primary difference between ZrB_2 and Si_3N_4 during SPS is the current flow within the tooling. ZrB_2 is exposed to both joule heating and heat transfer through conduction, whereas Si_3N_4 is limited to heat transfer by conduction from the joule-heated graphite tooling. As a result, the current path for the two material systems is different, which influences the sample thermal gradients.

6.5.1.1 Current Density and Heat Transfer

ZrB_2 in a typical SPS configuration will have current flow through the sample and the die wall. This current flow will generate a current density profile that can vary radially depending on the conductivity of the sample, but in general, the current density across the sample and die wall is more uniform compared to insulators and decreases in the radial direction approaching the outer diameter of the die wall, which can be seen in **FIGURE 6.3a**. For Si_3N_4, current is forced to pass through the die wall, and similarly the current

density decreases in the radial direction. However, since it only travels through the die wall, areas of high concentrated current density are generated by the sample edges, seen in **FIGURE 6.4b**. Thus, tooling design, such as die wall thickness, significantly impacts the current density distribution and introduces the idea of current path manipulation to control the degree of joule heating near the sample.

Once current path has been established, the manner in which the assembly joule-heats is defined; however, there is simultaneous cooling from the steel rams which develops the vertical temperature gradient. With vertically symmetric tooling, the center is the hottest, regardless of the high current densities within the punch. Near the sample, heat conduction paths are primarily a factor of the mass of graphite tooling - more tooling will naturally develop larger sample temperature gradients for both an electrical conductor and insulator. Hence, tooling mass can be added or subtracted to modify the heat transfer and current flow paths, but must be constrained to the mechanical capabilities of the material to withstand stresses (e.g. the die wall thickness is limited by the applied load of the run to withstand hoop and thermal stresses).

6.5.1.2 Effects of Contact Resistances on Current Path

Using a standard tooling configuration, current path can be manipulated by modifying contact resistances within the tooling. Through the addition of grafoil layers above and below the ZrB_2 disc, the path resistance increases and redirects current into the die wall. Alternatively, if additional foil layers are added surrounding the sample and die wall, there is increased localized heating at the foil interface which can be used to modify the sample temperature gradient. Due to interfaces near the sample being dominated by

grafoil contact resistances or thin insulating layers, graphite-graphite contact resistances are ignored.

The influence of tooling geometry and contact resistances on the current density and thermal gradients makes the scale-up process non-trivial, even going from a 20 mm to 30mm disc. However, with the fundamentals outlined above, we can use the model to predict the tooling and temperature needed for scale-up in SPS to produce uniform microstructures across the sintered part.

6.5.2 Modeling ZrB_2 (Electrical Conductor) Temperature Gradients and Experimental Validation of The Model

After defining the material properties and thermal and electric boundary conditions, experimental current values are input into the model and the thermal gradients are solved. The model has a high degree of accuracy with the experimentally measured values at the die wall, sample edge, and electrode (**TABLE 6.2**), validating the model for the 20 mm ZrB_2 disc. **FIGURE 6.3a** shows the model results with the current density of the sample at 75-90 A/cm^2 which results in a sample temperature gradient of 1985-2000 °C and a microstructure with a varying center to edge grain size. Grain size measurements across the diameter of the disc show the effects of the temperature gradient with a varying grain size of 13.2±6.0 μm at the center and 12.4±5.0 μm at the edge, which correlates with a hotter sample temperature at the center as predicted by the model (Error! Reference source not found.).

Using the same sintering conditions on a 30mm disc using SPS (T=1900°C, P=35MPa, dwell=5min) and 30mm tooling described in **TABLE 6.1**, the model identifies immediate differences in sample current density (100-115 A/cm^2) and temperature

gradient, as seen in **FIGURE 6.3b**. The predicted model sample temperature is 1950-1976°C, up to 50°C lower than needed to fully densify a 20 mm disc. Experimental application of the model results in a sample that is only 97% theoretical density with the porosity evident in the microstructure.

TABLE 6.2: Model and experimental temperature measurements for a 20mm disc.

	Measurement Location	**Experimental Value**	**Model Value**
ZrB_2	Current Input	1360 ± 22	1393
	Die Wall Temperature	1900	1899
	Sample Edge Temperature	1985	1985
	Electrode Temperature	410±20	397
Si_3N_4	Voltage Input	3.279 ± 0.256	3.19
	Die Wall Temperature	1701 ± 6	1701.25
	Sample Edge Temperature	1770	17
	Electrode Temperature	313	321

In order to obtain an identical microstructure on a 30 mm disc, the die wall temperature is increased to 1940°C and grafoil contact resistances are added between spacers to reduce the sample current density (81-90 A/cm^2), as shown in **FIGURE 6.3c**. The model predicted sample temperature gradient of 1985-2004°C, and the measured grain size at the center (13.8 μm) and edge grain (12.3 μm) matches the 20mm disc (Error! Reference source not found.).

6.5.3 Modeling Si_3N_4 (Electrical Insulator) Temperature Gradients and Experimental Validation of the Model

When Si_3N_4 material properties are input and gradients are solved, as seen in Table 2, the model voltage of 3.40 V and subsequent die wall temperature of 1699 °C demonstrates a high degree of accuracy with experimentally recorded values. The model (Figure 4.a) predicts a sample temperature gradient of 11 °C with the sample center at 1746°C and the edge at 1734 °C. Due to the large die wall thickness, the temperature at the sample center is highest. Average grain size measurements of 359.2 ± 194.1 nm and 320.4 ± 144.7 nm, at the sample center and edge respectively, confirm the trend in sample temperature gradient predicted by the model. Large grain size deviations are reported due to the high aspect ratio of β-Si3N4. Figure 5 plots wt% β-Si3N4 with respect to radial position with <6% wt% β-Si3N4 variation across the diameter.

TABLE 6.3: ZrB_2 and Si_3N_4 modeled sample temperatures with experimentally measured grain size.

Material System	**Sample Size**	**Densification Temperature (Die Wall)**	**Center (r=0)**		**Edge (r=10, 15)**	
			Grain Size	Sample Temperature	Grain Size	Sample Temperature(°C)
ZrB_2	20mm	1900°C	13.2±6.0	2000 °C	12.4±5.0	1985 °C
	30mm (**Uniform**)	1900°C	13.8±5.1	2004 °C	12.3±4.9	1985 °C
	30mm (non-uniform)	1940°C	--	1966 °C	--	1945 °C
Si_3N_4	20mm	1700°C	354±179 nm	1732 °C	320 ± 145 nm	1726 °C
	30mm (**Uniform**)	1700°C	353±160 nm	1725 °C	305 ± 124 nm	1742 °C
	30mm (non-uniform)	1735°C	410±198 nm	1690 °C	349 ± 157 nm	1713 °C

Unlike the model for ZrB_2, modeled sample edge temperature of 1734 °C does not correlate well with direct sample temperature measurement of 1770 °C as seen in **TABLE 6.2**. For an insulating material all current is forced through the die wall, as seen in **FIGURE**

6.4, thus joule-heating is entirely dependent upon the graphite thermal and electrical properties. Thus, die wall temperature are incredibly sensitive to inaccuracies in graphite material properties when using Si_3N_4. The inaccuracy between model and experimental sample edge temperatures can be ascribed to a higher graphite thermal conductivity value used in the model. Acknowledging the discrepancy, we scale to a 30 mm disc and qualify the success of the scale up process.

To develop a uniform 30mm disc, the predicted tooling necessary requires an increase in the die wall temperature to 1735°C and reducing current density near the sample edge. Insulating spacers are used above and below the sample to reduce the localized current density at the sample edge. The modified tooling assembly and current density and temperature distributions can be seen in **FIGURE 6.4b** with a sample temperature gradient of 1734-1747 °C. Due to the thinner die wall thickness, the modeled sample edge temperature is predicted to be highest. Grain size measurements on the 30mm disc identifies the temperature gradients are similar to the 20mm disc with a grain size of 330±167 nm at the sample edge and 372±200 nm at the sample center. As seen in **FIGURE 6.5**, the deviation of β-Si_3N_4 only varies ~4% across the diameter of the disc; however, the average β-Si_3N_4 content value is higher.

The high model accuracy for ZrB_2 suggests Si_3N_4 and other electric insulators must use high accuracy measurements for graphite, as there is zero current flow through the sample. The model for Si_3N_4 is useful in predicting the temperature gradient across the part, but not the absolute value as experimentally measured. In upcoming work currently unpublished, we found β-content growth rate is dependent on the applied load, which can be influenced by thermal stresses in the tooling. To enhance the fidelity of the model with

Si_3N_4 and other insulators that have strong phase change decencies with local stress fields, a coupled thermal-electrical-mechanical model is needed.

6.5.4 Tooling Prediction for Uniform 100mm ZrB_2 and Si_3N_4 Discs

In order to scale-up to larger parts, electrical conductors and electrical insulators) require different approaches to obtain uniform microstructural properties. Using the model designed in the SPS 10-3 and translated to a larger DCS 100-36 system (DCS100-36, 36000A, 12V, 100 ton hydraulic, continuous DC, Thermal Technologies, Santa Rosa, CA, USA) available to our research group at the University of Arizona, we can evaluate a first iteration model using various tooling configurations before calibrating the model to the specific equipment.

ZrB_2 has difficulty maintaining uniform temperature gradients due to excessive overheating in the center of the sample. Presented in **Figure 6.6a** is a tooling design that shows promise in reducing the temperature gradient while still exposing a 100mm ZrB_2 disc to current density. The tooling uses a hollow punch design which localizes current density near the sample edge, which is typically overcooled using a solid punch design, while the spacers around the sample allows minimal current flow through the sample center. Thus, by manipulating current to provide localized heating at the sample edge, we can produce a uniform sample temperature gradient 1988-2010°C.

Si_3N_4, in contrast to ZrB_2, is heated solely by conduction and experiences overcooled centers with high sample edge temperatures. Current density is manipulated to force localized hot spots near the center through a T-shaped punch, which allows the center

to be heated. Using the T-punch design, we predict a sample edge to center temperature of 1769-1776°C (**Figure 6.6b**).

6.5.5 Model Comparison to Literature

In order to determine the effectiveness of our model, we compare it to a model developed by Giuntini et al. [100] who have modified tooling resistances on a 62mm Si_3N_4 disc to obtain high uniformity using an FCT system (FCT HPD25, FCT Systeme GmbH, Frankenblick, Germany). Through slight modification of the contact resistance, they predict a decrease in temperature gradient from 210°C to 45°C. Replicating their tooling design and placement of the insulating layer to include our thermal and electrical boundary conditions, we are unable to achieve significant part uniformity, however, the temperature gradient across our modeled part does decrease, from 100°C to 90°C. This discrepancy is most likely due to the variation in material properties, contact resistances, and the current/voltage values displayed by the machine, which will change the degree and location of localized heating and heat transfer within the tooling assembly. This unfortunately shows that SPS models are not universal and must be calibrated for each system used and boundary conditions solved to obtain the highest fidelity model.

6.6 Summary and Conclusions

A thermal-electrical coupled finite element based model is developed to represent tooling in a 2D axisymmetric model. The model is validated on a 20mm disc using both ZrB_2, an electrical conductor, and Si_3N_4, an electrical insulator, and used to engineer tooling that predicts uniform large-scale parts. Electrical conductors allow current flow through the sample, and when scaling to larger diameters, the center is overheated and generates large temperature gradients that dissipate from center to edge. Electrical

insulators are heated solely by conduction from the die forcing current densities to localize around the sample edge which generates temperature gradients with a maximum at the edge – temperature gradients for insulators also depends on die thickness. A ZrB_2 20mm disc is scaled to 30mm to have identical microstructural uniformity with a center to edge average grain size of ~13.5 μm to ~12.4 μm by reducing sample current density using grafoil interfaces that encourages current to flow through the die wall. Similarly, 20mm and 30mm Si_3N_4 discs were produced to have uniform β-Si_3N_4 content across the diameter, which is sensitive to temperature distributions by moving localized current densities away from the sample edge. With an understanding of the basics of current manipulation, we propose tooling necessary to produce uniform 100mm ZrB_2 and Si_3N_4 discs. Due to differences in tooling and interface resistances, models are not universal, and it is recommended that each model be calibrated and developed for your system to obtain the highest fidelity model.

6.7 Acknowledgement

A National Science Foundation Early Faculty Career Award under Division of Materials Research-0954110 supports material processing of ceramics using spark plasma sintering. Authors thank L.S. Walker and W. Pinc for preliminary model development.

6.8 Figures

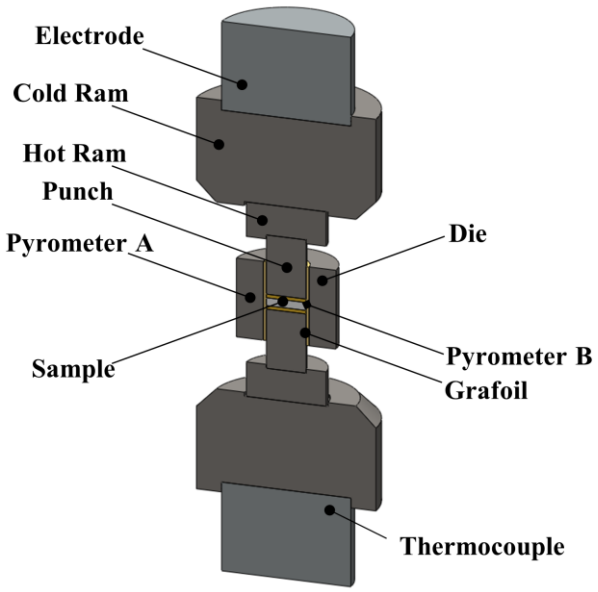

FIGURE 6.1: Schematic of 20mm SPS tooling shows the electrodes, graphite tooling, grafoil layers, pyrometer sighting locations, and the sample.

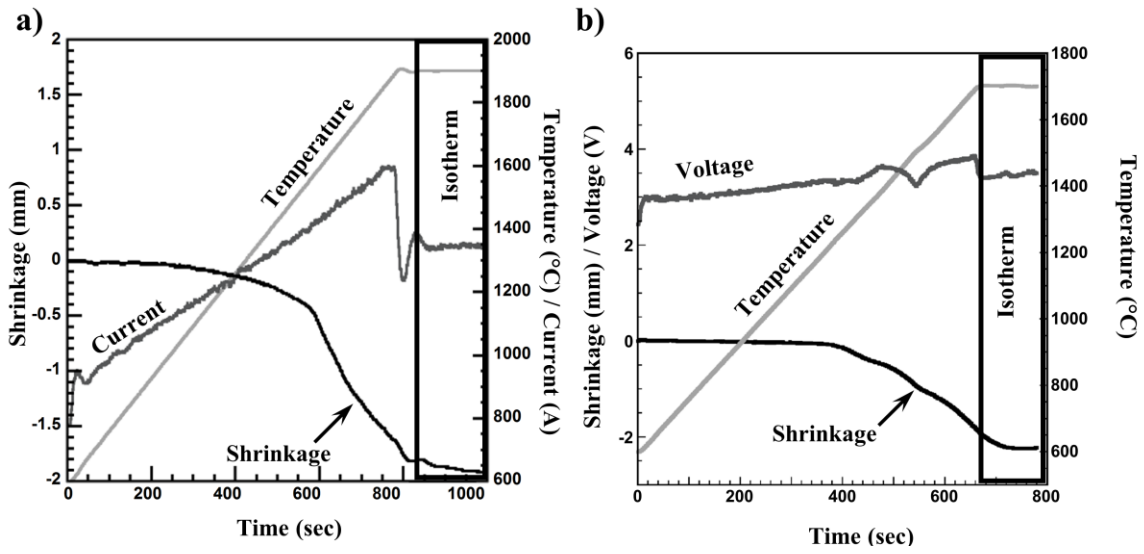

FIGURE 6.2: Densification profiles show the temperature, current/voltage and shrinkage for a) ZrB_2 and b) *Si_3N_4 values that are used as model inputs.

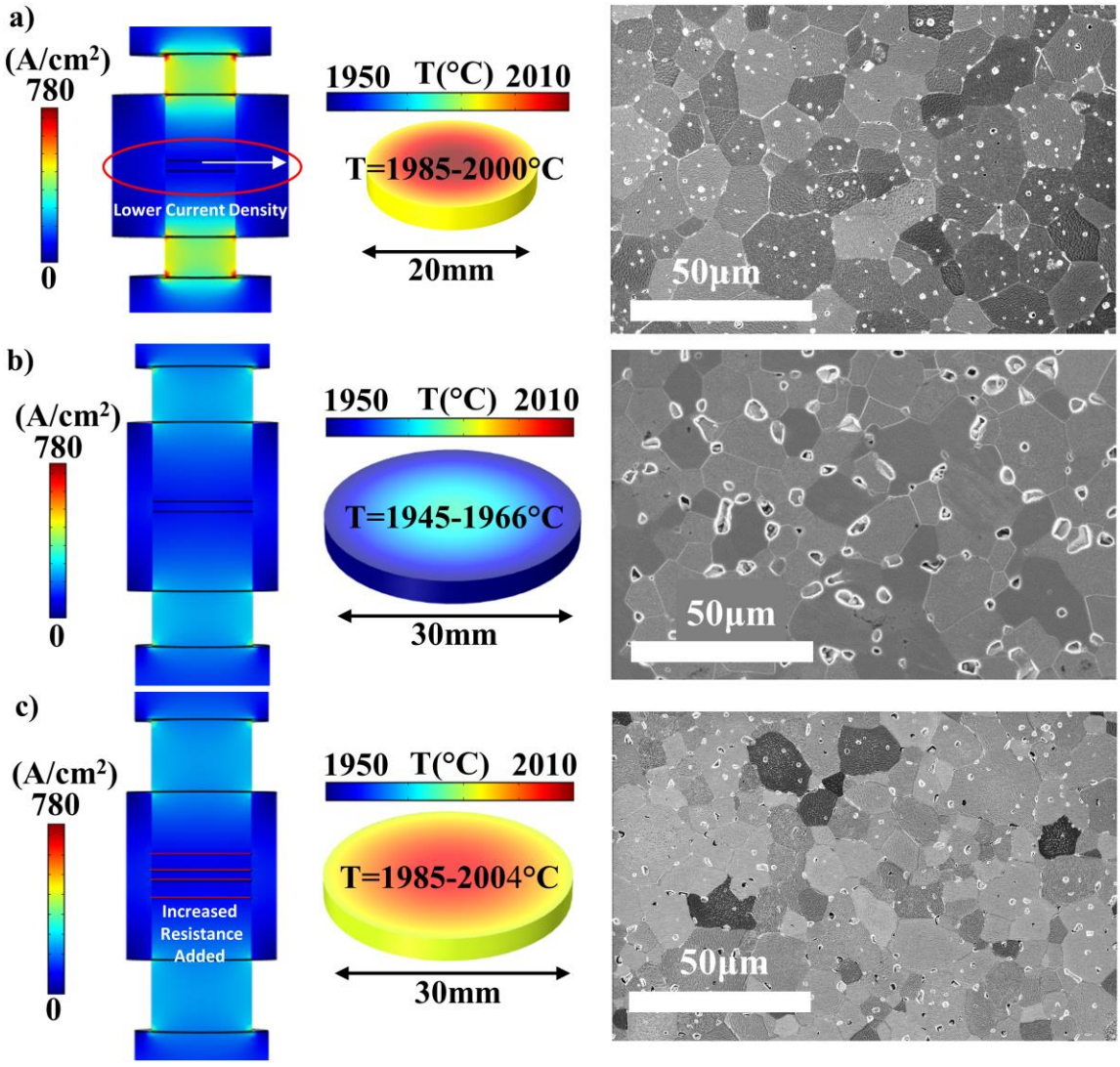

FIGURE 6.3: Tooling used to produce the current density maps that results in the sample temperature gradients and center microstructure (etched) for a) high density 20mm ZrB_2, b) non-uniform and low density 30mm ZrB_2, and c) high density 30mm ZrB_2 discs.

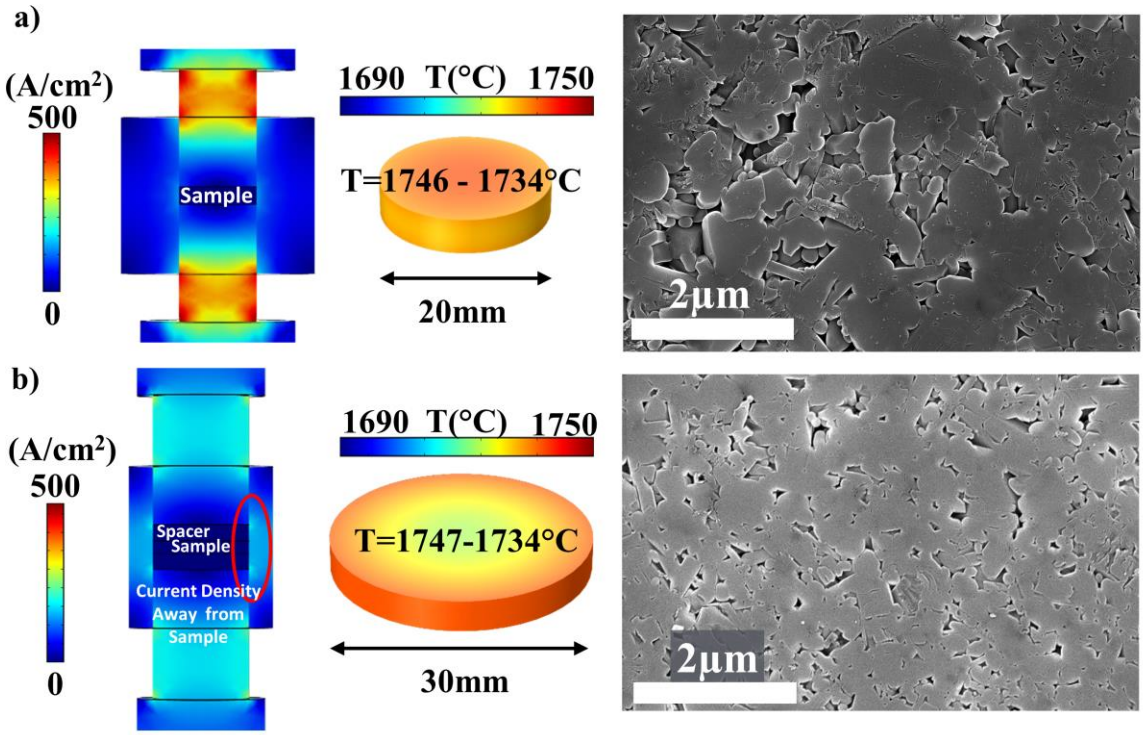

FIGURE 6.4: Tooling used to produce the current density maps that results in the sample temperature gradients and center microstructure for a) uniform 20mm Si_3N_4 and b) uniform 30mm Si_3N_4 discs.

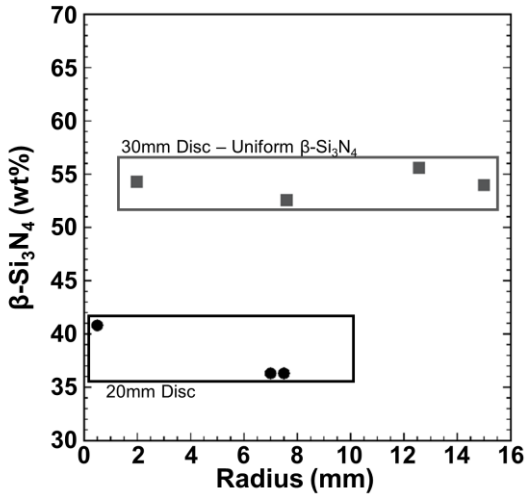

FIGURE 6.5: XRD analysis is used to measure β-Si_3N_4 in 20 mm and 30 mm discs as a function of radial position. Using the model, we improve the temperature uniformity across the 30mm part to a β-Si_3N_4 variation of 5%.

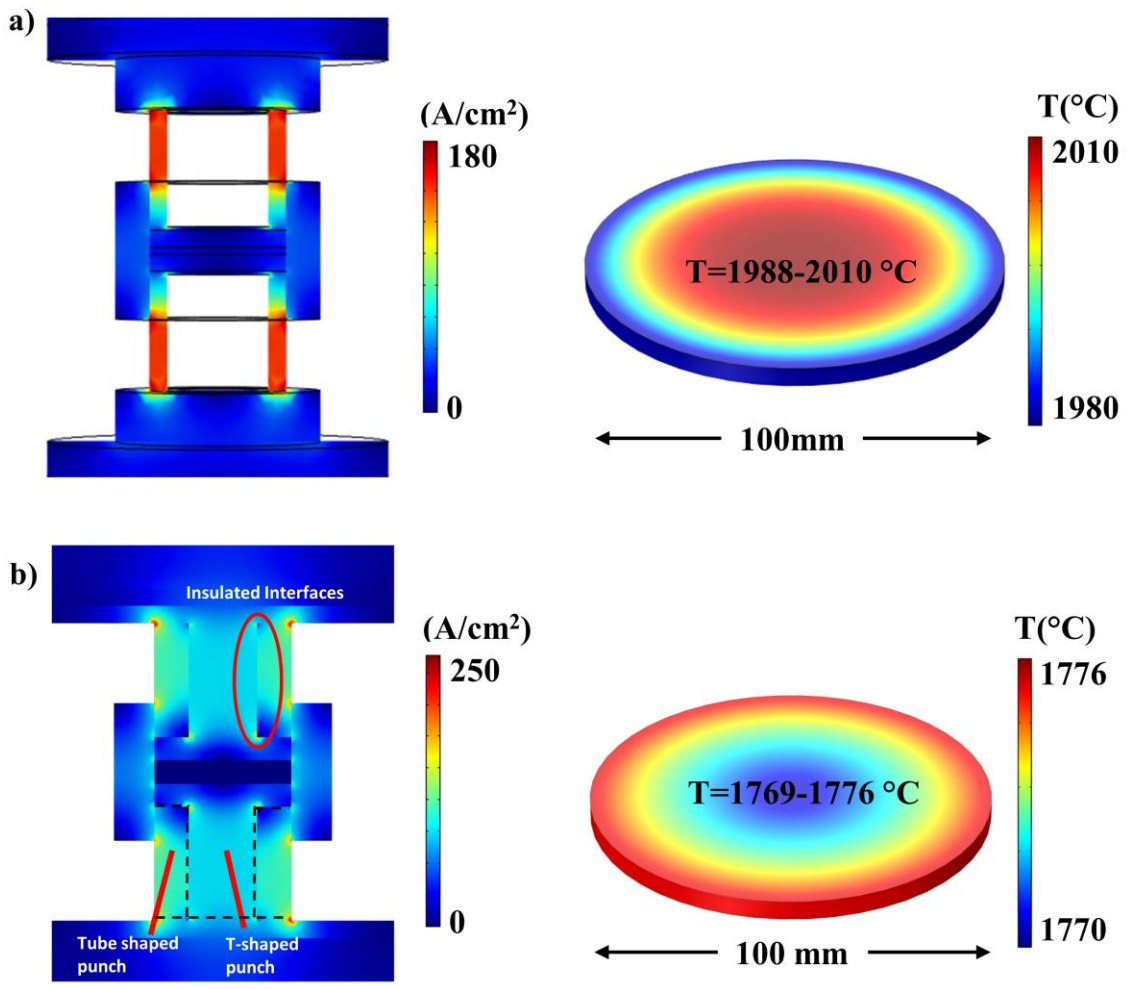

FIGURE 6.6: Model predictions showing the tooling used to minimize temperature gradients in a) ZrB_2 by focusing current density by the sample edge and b) Si_3N_4 by introducing localized current density hot spots near the sample center.

6.9 Modeling Material Properties

Reported here are thermal and electrical properties used in the model. Each material is defined with properties as a function of temperature in piecewise format.

Graphite

Thermal Conductivity [kT(W/(m·K))]:

$110.12 - 0.135\,\mathbf{T} + 8E\text{-}5\,\mathbf{T}^2 - 1E\text{-}8\,\mathbf{T}^3$ (273<T<673)

$78 - 0.046\,\mathbf{T} + 1E\text{-}5\,\mathbf{T}^2$ (673<T<1600)

$39 - 0.006\,\mathbf{T}$ (1600<T<3000)

Electrical Conductivity [σ(S/m)]:

$2.147E4 + 2.1589\,\mathbf{T} - 0.159\,\mathbf{T}^2 + 4.0E\text{-}5\,\mathbf{T}^3 - 3.0E\text{-}9\,\mathbf{T}^4$ (273<T<2200)

$1.7E5 - 40.406\,\mathbf{T}$ (2200<T<3500)

Heat Capacity [cp(J/(kg·K))]:

$491.9\,\mathrm{Log}(\mathbf{T}) - 2016$ (273<T<3000)

Emmisivity:

0.85

ZrB_2

Thermal Conductivity [kT(W/(m·K))]:

$83.42 + 0.00135\,\mathbf{T} - 4.29E\text{-}6\,\mathbf{T}^2 + 9.90\,\mathbf{T}^3$ (293<T<2273)

Electrical Conductivity [σ(S/m)]:

$5.0E\text{-}6 - 3760\,\mathbf{T} + 0.958\,\mathbf{T}^2$ (293<T<1900)

$1.56E6 - 100\,\mathbf{T}$ (1900<T<3000)

Heat Capacity [cp(J/(kg·K))]:

$585.45 + 0.156\,\mathbf{T} - 1.30E7\,\mathbf{T}^2$ (283<T<1200)

Si_3N_4

Thermal Conductivity [kT(W/(m·K))]:

$6502.29\,\mathbf{T}^{-0.7}$ (293<T<2273)

Electrical Conductivity [σ(S/m)]:

10-4 (All T)

Heat Capacity [cp(J/(kg·K))]:

$$422.76 + 1.078\,\mathbf{T} - 4.0\text{E-}4\,\mathbf{T}^2 + 6.0\text{E-}8\,\mathbf{T}^3 \qquad (300<T<3000)$$

321 Stainless Steel

Thermal Conductivity [kT(W/(m·K))]:

$$0.298 + 0.152\,\mathbf{T} - 6.87\text{E-}4\,\mathbf{T}^2 + 1.163\text{E-}6\,\mathbf{T}^3 \qquad (273<T<1672)$$

Electrical Conductivity [σ(S/m)]:

$$(4.873\text{E-}7 + 9.825\text{E-}10\,\mathbf{T} - 3.252\text{E-}13\,\mathbf{T}^2 - 4.485\text{E-}17\,\mathbf{T}^3 + 3.914\text{E-}20\,\mathbf{T}^4)^{-1} \qquad (293<T<1672)$$

Heat Capacity [cp(J/(kg·K))]:

$$235.65 + 1.3\,\mathbf{T} - 0.0019\,\mathbf{T}^2 + 1.348\text{E-}6\,\mathbf{T}^3 - 3.343\text{E-}10\,\mathbf{T}^4 \qquad (300<T1500)$$

Emmisivity:

0.5

CHAPTER 7

SUMMARY AND FUTURE WORK

7.1 Densification and Thermodynamic Processing of UHTCs

A thermodynamically-driven approach is used to enhance ZrB_2 powder purity. Using the method of identifying the amount of each oxide species (ZrO_2 and B_2O_3) that forms on the powder surface, we can calculate and determine the minimum amount of oxide reducing agent needed to reduce surface oxides using carbon and B_4C.

Carbon additions have the ability to reduce powder surface oxides, however, the reduction reaction that forms Zr(C,O) limits the cleaning potential. Discreet microstructural impurities of ZrO_2 are predicted to precipitate from the seeding of Zr(C,O) throughout the microstructure. Carbon from Zr(C,O) dissolves into the ZrB_2 grain at high temperatures and discreet ZrO_2 that has no solubility with ZrB_2 can then be found using STEM after SPS.

B_4C additions of 0.25wt% are used to reduce ZrB_2 surface oxides to a minimum. Due to oxide reduction being a function of the B_4C and ZrO_2 diffusion length, B_4C can be used in less than stoichiometric quantities to reduce powder surface oxides to a minimum. After SPS, the resulting ceramic has very low oxygen impurities of only 0.06wt%. With a very low Zr-B oxide content in the microstructure, “trash collector” oxides are found composed of manufacturer powder impurities. The high purity ZrB_2 has very small grain size with superior room temperature mechanical properties.

In future work, the thermodynamic cleaning approach used on ZrB_2 can be translated to other metal diborides with similar oxide chemistries. ZrB_2 mechanical

properties at elevated temperatures up to 2000°C also need to be evaluated to determine the effects of oxide impurities on strength. Further thermodynamic analysis must be performed to extend the cleaning methodology to more relevant UHTC composite systems like ZrB_2+SiC.

7.2 Large-Scale Modeling

A finite element analysis based model is developed to predict sample temperature uniformities of ZrB_2 and Si_3N_4. The model is built on experimental runs of small-scale 20mm discs. The model is used to produce uniform 30mm discs and advanced tooling predictions to produce 100 mm discs of ZrB_2 and Si_3N_4. The model shows high fidelity with ZrB_2 experiments showing grain size distributions, and hence temperature distributions, for the 20mm and 30mm disc are nearly identical. Unfortunately, the Si3N4 showed discrepancies that can be caused by innacurate graphite properties. Because the electrical conductivity of ZrB_2 and graphite are in the same order of magnitude, the graphite material properties do not evolve into large errors. However, since all the current density flows through the graphite when densifying Si_3N_4, the temperature gradients are more sensitive to material property errors.

In future work, the model needs to evolve to describe the entire sintering process through the development of a time-dependent, or transient, model. Accurate graphite material properties need to be obtained in order to enhance the fidelity when modeling electrical insulators. Lastly, the model needs to incorporate a thermal-electrical-mechanical couple for materials that are sensitive to phase changes due to stress fields as well as complex geometries.

REFERENCES

[1] F. Zuniga, S. Cliff, D. Kinney, V. Hawke, C. Tang, and S. Smith, "Vehicle Design of a Sharp CTV Concept Using a Virtual Flight Rapid Integration Test Environment;" in *AIAA Atmospheric Flight Mech. Conf. Exhib.* American Institute of Aeronautics and Astronautics, n.d.

[2] T.H. Squire and J. Marschall, "Material property requirements for analysis and design of UHTC components in hypersonic applications," *J. Eur. Ceram. Soc.*, **30** [11] 2239–2251 (2010).

[3] E. Wuchina, E. Opila, M. Opeka, W. Fahrenholtz, and I. Talmy, "UHTCs: Ultra-high temperature ceramic materials for Extreme Environment Applications," *Interface-Electrochem. Soc.*, **16** [4] 30–36 (2007).

[4] W.G. Fahrenholtz, G.E. Hilmas, I.G. Talmy, and J.A. Zaykoski, "Refractory Diborides of Zirconium and Hafnium," *J. Am. Ceram. Soc.*, **90** [5] 1347–1364 (2007).

[5] B. Yang, J. Li, B. Zhao, Y. Hu, T. Wang, D. Sun, R. Li, S. Yin, *et al.*, "Synthesis of hexagonal-prism-like ZrB2 by a sol–gel route," *Powder Technol.*, **256** 522–528 (2014).

[6] L.S. Walker and E.L. Corral, "Structural Influence on the Thermal Conversion of Self-Catalyzed HfB2/ZrB2 Sol–Gel Precursors by Rapid Ultrasonication of Oxychloride Hydrates," *J. Am. Ceram. Soc.*, **97** [2] 399–406 (2014).

[7] Y. Zhang, R. Li, Y. Jiang, B. Zhao, H. Duan, J. Li, and Z. Feng, "Morphology evolution of ZrB2 nanoparticles synthesized by sol–gel method," *J. Solid State Chem.*, **184** [8] 2047–2052 (2011).

[8] H. Ji, M. Yang, M. Li, G. Ji, H. Fan, and X. Sun, "Low-temperature synthesis of ZrB2 nano-powders using a sorbitol modified sol–gel processing route," *Adv. Powder Technol.*, **25** [3] 910–915 (2014).

[9] H. Zhang, Y.J. Yan, Z.R. Huang, X.J. Liu, and D.L. Jiang, "Pressureless Sintering of ZrB2-SiC Ceramics Incorporating Sol-Gel Synthesized Ultra-Fine Ceramic Powders," *Key Eng. Mater.*, **434-435** 193–196 (2010).

[10] A.L. Chamberlain, W.G. Fahrenholtz, G.E. Hilmas, and D.T. Ellerby, "High-Strength Zirconium Diboride-Based Ceramics," *J. Am. Ceram. Soc.*, **87** [6] 1170–1172 (2004).

[11] J.W. Zimmermann, G.E. Hilmas, W.G. Fahrenholtz, R.B. Dinwiddie, W.D. Porter, and H. Wang, "Thermophysical Properties of ZrB2 and ZrB2–SiC Ceramics," *J. Am. Ceram. Soc.*, **91** [5] 1405–1411 (2008).

[12] L.-J. Yang, S.-Z. Zhu, Q. Xu, Z.-Y. Yan, and L. Liu, "Synthesis of ultrafine ZrB2 powders by sol-gel process," *Front. Mater. Sci. China*, **4** [3] 285–290 (2010).

[13] E.W. Neuman, G.E. Hilmas, and W.G. Fahrenholtz, "Mechanical behavior of zirconium diboride–silicon carbide–boron carbide ceramics up to 2200 °C," *J. Eur. Ceram. Soc.*, **35** [2] 463–476 (2015).

[14] C. Ang, T. Williams, D. Vowles, C. Wood, A. Seeber, and Y.-B. Cheng, "Influence of sol–gel derived ZrO2 and ZrC additions on microstructure and properties of ZrB2 composites," *J. Eur. Ceram. Soc.*, **34** [13] 3139–3149 (2014).

[15] S. Baik and P.F. Becher, "Effect of Oxygen Contamination on Densification of TiB2," *J. Am. Ceram. Soc.*, **70** [8] 527–530 (1987).

[16] M. Thompson, W.G. Fahrenholtz, and G. Hilmas, "Effect of Starting Particle Size and Oxygen Content on Densification of ZrB2," *J. Am. Ceram. Soc.*, **94** [2] 429–435 (2011).

[17] Y. Yan, Z. Huang, S. Dong, and D. Jiang, "New Route to Synthesize Ultra-Fine Zirconium Diboride Powders Using Inorganic–Organic Hybrid Precursors," *J. Am. Ceram. Soc.*, **89** [11] 3585–3588 (2006).

[18] S. Venugopal, A. Paul, B. Vaidhyanathan, J. Binner, A. Heaton, and P. Brown, "Nano-Crystalline Ultra High Temperature HfB2 and HfC Powders and Coatings using a Sol-Gel Approach;" pp. 151–159 in *Adv. Ceram. Coat. Mater. Extreme Environ.* Edited by D. Zhu, H.-T. Lin, Y. Zhou, S. Widjaja and D. Singh. John Wiley & Sons, Inc., 2011.

[19] G.J.K. Harrington, G.E. Hilmas, and W.G. Fahrenholtz, "Effect of Carbon and Oxygen on the Densification and Microstructure of Hot Pressed Zirconium Diboride," *J. Am. Ceram. Soc.*, **96** [11] 3622–3630 (2013).

[20] L.S. Walker, W.R. Pinc, and E.L. Corral, "Powder Processing Effects on the Rapid Low-Temperature Densification of ZrB2–SiC Ultra-High Temperature Ceramic Composites Using Spark Plasma Sintering," *J. Am. Ceram. Soc.*, **95** [1] 194–203 (2012).

[21] J.R. Soulen, P. Sthapitanonda, and J.L. Margrave, "Vaporization of Inorganic Substances: B2O3, TeO2 and Mg3N2," *J. Phys. Chem.*, **59** [2] 132–136 (1955).

[22] W.G. Fahrenholtz, G.E. Hilmas, S.C. Zhang, and S. Zhu, "Pressureless Sintering of Zirconium Diboride: Particle Size and Additive Effects," *J. Am. Ceram. Soc.*, **91** [5] 1398–1404 (2008).

[23] S.C. Zhang, G.E. Hilmas, and W.G. Fahrenholtz, "Pressureless Densification of Zirconium Diboride with Boron Carbide Additions," *J. Am. Ceram. Soc.,* **89** [5] 1544–1550 (2006).

[24] S. Zhu, W.G. Fahrenholtz, G.E. Hilmas, and S.C. Zhang, "Pressureless sintering of carbon-coated zirconium diboride powders," *Mater. Sci. Eng. A,* **459** [1–2] 167–171 (2007).

[25] A.L. Chamberlain, W.G. Fahrenholtz, and G.E. Hilmas, "Pressureless Sintering of Zirconium Diboride," *J. Am. Ceram. Soc.,* **89** [2] 450–456 (2006).

[26] B. Post, F.W. Glaser, and D. Moskowitz, "Transition metal diborides," *Acta Metall.,* **2** [1] 20–25 (1954).

[27] H. Zhang, Y. Yan, Z. Huang, X. Liu, and D. Jiang, "Pressureless sintering of ZrB2–SiC ceramics: the effect of B4C content," *Scr. Mater.,* **60** [7] 559–562 (2009).

[28] S.-Q. Guo, T. Nishimura, Y. Kagawa, and J.-M. Yang, "Spark Plasma Sintering of Zirconium Diborides," *J. Am. Ceram. Soc.,* **91** [9] 2848–2855 (2008).

[29] S.-Q. Guo, "Densification of ZrB2-based composites and their mechanical and physical properties: A review," *J. Eur. Ceram. Soc.,* **29** [6] 995–1011 (2009).

[30] V. Zamora, A.L. Ortiz, F. Guiberteau, and M. Nygren, "Spark-plasma sintering of ZrB2 ultra-high-temperature ceramics at lower temperature via nanoscale crystal refinement," *J. Eur. Ceram. Soc.,* **32** [10] 2529–2536 (2012).

[31] O. Guillon, J. Gonzalez-Julian, B. Dargatz, T. Kessel, G. Schierning, J. Räthel, and M. Herrmann, "Field-Assisted Sintering Technology/Spark Plasma Sintering: Mechanisms, Materials, and Technology Developments," *Adv. Eng. Mater.,* **16** [7] 830–849 (2014).

[32] J.E. Alaniz, J.R. Morales, and J.E. Garay, “The current activated pressure assisted densification technique for producing nanocrystalline materials,” *JOM*, **62** [2] 58–62 (2010).

[33] J.H. Chae, K.H. Kim, Y.H. Choa, J. Matsushita, J.-W. Yoon, and K.B. Shim, “Microstructural evolution of Al2O3–SiC nanocomposites during spark plasma sintering,” *J. Alloys Compd.*, **413** [1–2] 259–264 (2006).

[34] Z.J. Shen and M. Nygren, “Non-Equilibrium Processing of Ceramics,” *Key Eng. Mater.*, **247** 79–82 (2003).

[35] F. Zhang, M. Reich, O. Kessler, and E. Burkel, “The potential of rapid cooling spark plasma sintering for metallic materials,” *Mater. Today*, **16** [5] 192–197 (2013).

[36] T. Mizuguchi, S. Guo, and Y. Kagawa, “Transmission electron microscopy characterization of spark plasma sintered ZrB2 ceramic,” *Ceram. Int.*, **36** [3] 943–946 (2010).

[37] L. Silvestroni and D. Sciti, “TEM analysis, mechanical characterization and oxidation resistance of a highly refractory ZrB2 composite,” *J. Alloys Compd.*, **602** 346–355 (2014).

[38] D.D. Jayaseelan, Y. Wang, G.E. Hilmas, W. Fahrenholtz, P. Brown, and W.E. Lee, “TEM investigation of hot pressed -10 vol.%SiC–ZrB2 composite,” *Adv. Appl. Ceram.*, **110** [1] 1–7 (2011).

[39] S. Brunauer, P.H. Emmett, and E. Teller, “Adsorption of gases in multimolecular layers,” *J. Am. Chem. Soc.*, **60** 309–319 (1938).

[40] Z.A. Munir, U. Anselmi-Tamburini, and M. Ohyanagi, "The effect of electric field and pressure on the synthesis and consolidation of materials: A review of the spark plasma sintering method," *J. Mater. Sci.*, **41** [3] 763–777 (2006).

[41] S.L. Dole, S. Prochazka, and R.H. Doremus, "Microstructural Coarsening During Sintering of Boron Carbide," *J. Am. Ceram. Soc.*, **72** [6] 958–966 (1989).

[42] C.M. Kapadia and M.H. Leipold, *The mechanism of grain growth in ceramics*. 1972.

[43] G. Zhao, X. Zhang, Z. Shen, D. Zhang, C. Hong, J. Li, and Z. Zhang, "Oxidation of ZrB2 Nanoparticles at High Temperature under Low Oxygen Pressure," *J. Am. Ceram. Soc.*, **97** [8] 2360–2363 (2014).

[44] F. Maglia, I.G. Tredici, G. Spinolo, and U. Anselmi-Tamburini, "Low temperature proton conduction in bulk nanometric TiO2 prepared by high-pressure field assisted sintering," *J. Mater. Res.*, **27** [15] 1975–1981 (2012).

[45] T. Yamamoto, H. Kitaura, Y. Kodera, T. Ishii, M. Ohyanagi, and Z.A. Munir, "Consolidation of Nanostructured β-SiC by Spark Plasma Sintering," *J. Am. Ceram. Soc.*, **87** [8] 1436–1441 (2004).

[46] R. Chaim and M. Margulis, "Densification maps for spark plasma sintering of nanocrystalline MgO ceramics," *Mater. Sci. Eng. A*, **407** [1–2] 180–187 (2005).

[47] E.A. Olevsky and L. Froyen, "Impact of Thermal Diffusion on Densification During SPS," *J. Am. Ceram. Soc.*, **92** S122–S132 (2009).

[48] H. Conrad, "Effects of electric current on solid state phase transformations in metals," *Mater. Sci. Eng. A*, **287** [2] 227–237 (2000).

[49] C.S. Bonifacio, T.B. Holland, and K. van Benthem, “Time-dependent dielectric breakdown of surface oxides during electric-field-assisted sintering,” *Acta Mater.,* **63** 140–149 (2014).

[50] T.B. Holland, U. Anselmi-Tamburini, D.V. Quach, T.B. Tran, and A.K. Mukherjee, “Local field strengths during early stage field assisted sintering (FAST) of dielectric materials,” *J. Eur. Ceram. Soc.,* **32** [14] 3659–3666 (2012).

[51] J.F. Verweij and J.H. Klootwijk, “Dielectric breakdown I: A review of oxide breakdown,” *Microelectron. J.,* **27** [7] 611–622 (1996).

[52] X. Song, X. Liu, and J. Zhang, “Neck Formation and Self-Adjusting Mechanism of Neck Growth of Conducting Powders in Spark Plasma Sintering,” *J. Am. Ceram. Soc.,* **89** [2] 494–500 (2006).

[53] E. Zapata-Solvas, D.D. Jayaseelan, H.T. Lin, P. Brown, and W.E. Lee, “Mechanical properties of ZrB2- and HfB2-based ultra-high temperature ceramics fabricated by spark plasma sintering,” *J. Eur. Ceram. Soc.,* **33** [7] 1373–1386 (2013).

[54] S.C. Zhang, G.E. Hilmas, and W.G. Fahrenholtz, “Mechanical properties of sintered ZrB2–SiC ceramics,” *J. Eur. Ceram. Soc.,* **31** [5] 893–901 (2011).

[55] D. Sciti, F. Monteverde, S. Guicciardi, G. Pezzotti, and A. Bellosi, “Microstructure and mechanical properties of ZrB2–MoSi2 ceramic composites produced by different sintering techniques,” *Mater. Sci. Eng. A,* **434** [1–2] 303–309 (2006).

[56] M.J. Thompson, W.G. Fahrenholtz, and G.E. Hilmas, “Elevated Temperature Thermal Properties of ZrB2 with Carbon Additions,” *J. Am. Ceram. Soc.,* **95** [3] 1077–1085 (2012).

[57] D. Pham, M. V.R., K. Muralidharan, and E.L. Corral, “Spark plasma sintering of zirconium diboride using carbon as an oxide reducing agent. Part 1: Densification behavior and microstructural analysis,” *J. Eur. Ceram. Soc.*, (2015).

[58] A. Fernández Guillermet, “Analysis of thermochemical properties and phase stability in the zirconium-carbon system,” *J. Alloys Compd.*, **217** [1] 69–89 (1995).

[59] M. Chen, B. Hallstedt, and L.J. Gauckler, “Thermodynamic modeling of the ZrO2–YO1.5 system,” *Solid State Ion.*, **170** [3–4] 255–274 (2004).

[60] S.K. Sarkar, A.D. Miller, and J.I. Mueller, “Solubility of Oxygen in ZrC,” *J. Am. Ceram. Soc.*, **55** [12] 628–630 (1972).

[61] M. Gendre, A. Maître, and G. Trolliard, “Synthesis of zirconium oxycarbide (ZrCxOy) powders: Influence of stoichiometry on densification kinetics during spark plasma sintering and on mechanical properties,” *J. Eur. Ceram. Soc.*, **31** [13] 2377–2385 (2011).

[62] S.N. Karlsdottir, J.W. Halloran, and A.N. Grundy, “Zirconia Transport by Liquid Convection during Oxidation of Zirconium Diboride–Silicon Carbide,” *J. Am. Ceram. Soc.*, **91** [1] 272–277 (2008).

[63] E. Rudy and S. Windisch, *Ternary Phase Equilibria in Transition Metal-Boron-Carbon-Silicon Systems. Part II. Ternary Systems*. Air Force Materials Laboratory, Wright-Patterson Air Force Base, 1966.

[64] J.W. Lawson, C.W. Bauschlicher, and M. Daw, “Ab initio Computations of the Electronic, Mechanical, and Thermal Properties of Ultra High Temperature Ceramics (UHTC) ZrB2 and HfB2;” in Daytona Beach, FL, United States, 2011.

[65] M. Mallik, A.J. Kailath, K.K. Ray, and R. Mitra, "Electrical and thermophysical properties of ZrB2 and HfB2 based composites," *J. Eur. Ceram. Soc.*, **32** [10] 2545–2555 (2012).

[66] R. Licheri, R. Orrù, C. Musa, and G. Cao, "Combination of SHS and SPS Techniques for fabrication of fully dense ZrB2-ZrC-SiC composites," *Mater. Lett.*, **62** [3] 432–435 (2008).

[67] L. Yu, J. Yang, T. Qiu, D.D. Guo, L.M. Pan, and J.X. Zhang, "Microstructure and mechanical properties of (ZrB2+ZrC)/Zr3[Al(Si)]4C6 composites prepared by in situ hot-pressing," *Mater. Lett.*, **96** 188–191 (2013).

[68] O.N. Grigoriev, B.A. Galanov, V.A. Kotenko, S.M. Ivanov, A.V. Koroteev, and N.P. Brodnikovsky, "Mechanical properties of ZrB2–SiC(ZrSi2) ceramics," *J. Eur. Ceram. Soc.*, **30** [11] 2173–2181 (2010).

[69] J. Zou, G.-J. Zhang, C.-F. Hu, T. Nishimura, Y. Sakka, H. Tanaka, J. Vleugels, and O. Van der Biest, "High-temperature bending strength, internal friction and stiffness of ZrB2–20 vol% SiC ceramics," *J. Eur. Ceram. Soc.*, **32** [10] 2519–2527 (2012).

[70] E.W. Neuman, G.E. Hilmas, and W.G. Fahrenholtz, "Mechanical behavior of zirconium diboride–silicon carbide ceramics at elevated temperature in air," *J. Eur. Ceram. Soc.*, **33** [15–16] 2889–2899 (2013).

[71] W.-M. Guo and G.-J. Zhang, "New Borothermal Reduction Route to Synthesize Submicrometric ZrB2 Powders with Low Oxygen Content," *J. Am. Ceram. Soc.*, **94** [11] 3702–3705 (2011).

[72] R. Li, Y. Zhang, H. Lou, J. Li, and Z. Feng, "Synthesis of ZrB2 nanoparticles by sol-gel method," *J. Sol-Gel Sci. Technol.*, **58** [2] 580–585 (2011).

[73] H.J. Brown-Shaklee, W.G. Fahrenholtz, and G.E. Hilmas, "Densification Behavior and Thermal Properties of Hafnium Diboride with the Addition of Boron Carbides," *J. Am. Ceram. Soc.*, **95** [6] 2035–2043 (2012).

[74] W.-M. Guo and G.-J. Zhang, "Reaction Processes and Characterization of ZrB2 Powder Prepared by Boro/Carbothermal Reduction of ZrO2 in Vacuum," *J. Am. Ceram. Soc.*, **92** [1] 264–267 (2009).

[75] H.M. Chen, F. Zheng, H.S. Liu, L.B. Liu, and Z.P. Jin, "Thermodynamic assessment of B–Zr and Si–Zr binary systems," *J. Alloys Compd.*, **468** [1–2] 209–216 (2009).

[76] A. Saengdeejing, J.E. Saal, V.R. Manga, and Z.-K. Liu, "Defects in boron carbide: First-principles calculations and CALPHAD modeling," *Acta Mater.*, **60** [20] 7207–7215 (2012).

[77] V.R. Manga, D. Pham, E.L. Corral, and K. Muralidharan, "Thermodynamic Description of the Zr-B-C-O Quaternary Phase Diagram," *CALPHAD*, (2015).

[78] G. r. Anstis, P. Chantikul, B. r. Lawn, and D. b. Marshall, "A Critical Evaluation of Indentation Techniques for Measuring Fracture Toughness: I, Direct Crack Measurements," *J. Am. Ceram. Soc.*, **64** [9] 533–538 (1981).

[79] H.J. Brown-Shaklee, W.G. Fahrenholtz, and G.E. Hilmas, "Densification Behavior and Microstructure Evolution of Hot-Pressed HfB2," *J. Am. Ceram. Soc.*, **94** [1] 49–58 (2011).

[80] S.S. Ordan'yan, A.I. Dmitriev, K.T. Bizhev, and E.K. Stepanenko, "Interaction in the system B4C-ZrB2," *Powder Metall. Met. Ceram.*, **27** [1] 38–40 (1988).

[81] A.M. Locci, R. Orrù, G. Cao, and Z.A. Munir, "Simultaneous Spark Plasma Synthesis and Densification of TiC–TiB2 Composites," *J. Am. Ceram. Soc.*, **89** [3] 848–855 (2006).

[82] N. Ni, S. Lozano-Perez, J. Sykes, and C. Grovenor, "Quantitative EELS analysis of zirconium alloy metal/oxide interfaces," *Ultramicroscopy*, **111** [2] 123–130 (2011).

[83] M. Terauchi, "Electronic structure analyses of BN network materials using high energy-resolution spectroscopy methods based on transmission electron microscopy," *Microsc. Res. Tech.*, **69** [7] 531–537 (2006).

[84] T. Sekiguchi, K. Kimoto, T. Aoyama, and Y. Mitsui, "Nitrogen Distribution and Chemical Bonding State Analyses in Oxynitride Film by Spatially Resolved Electron Energy Loss Spectroscopy (EELS)," *Jpn. J. Appl. Phys.*, **37** [6B] L694 (1998).

[85] R. Wirth, "Water in minerals detectable by electron energy-loss spectroscopy EELS," *Phys. Chem. Miner.*, **24** [8] 561–568 (1997).

[86] D. Kalish, E.V. Clougherty, and K. Kreder, "Strength, Fracture Mode, and Thermal Stress Resistance of HfB2 and ZrB2," *J. Am. Ceram. Soc.*, **52** [1] 30–36 (1969).

[87] A. Balbo and D. Sciti, "Spark plasma sintering and hot pressing of ZrB2–MoSi2 ultra-high-temperature ceramics," *Mater. Sci. Eng. A*, **475** [1–2] 108–112 (2008).

[88] V. Medri, F. Monteverde, A. Balbo, and A. Bellosi, "Comparison of ZrB2-ZrC-SiC Composites Fabricated by Spark Plasma Sintering and Hot-Pressing," *Adv. Eng. Mater.*, **7** [3] 159–163 (2005).

[89] A. Bellosi, F. Monteverde, and D. Sciti, "Fast Densification of Ultra-High-Temperature Ceramics by Spark Plasma Sintering," *Int. J. Appl. Ceram. Technol.*, **3** [1] 32–40 (2006).

[90] R. Chaim, "Densification mechanisms in spark plasma sintering of nanocrystalline ceramics," *Mater. Sci. Eng. A,* **443** [1–2] 25–32 (2007).

[91] J.E. Garay, U. Anselmi-Tamburini, and Z.A. Munir, "Enhanced growth of intermetallic phases in the Ni–Ti system by current effects," *Acta Mater.,* **51** [15] 4487–4495 (2003).

[92] T.T. Sasaki, T. Mukai, and K. Hono, "A high-strength bulk nanocrystalline Al–Fe alloy processed by mechanical alloying and spark plasma sintering," *Scr. Mater.,* **57** [3] 189–192 (2007).

[93] X.L. Shi, F.M. Xu, Z.J. Zhang, Y.L. Dong, Y. Tan, L. Wang, and J.M. Yang, "Mechanical properties of hot-pressed Al2O3/SiC composites," *Mater. Sci. Eng. A,* **527** [18–19] 4646–4649 (2010).

[94] X.L. Shi, G.Q. Shao, X.L. Duan, R.Z. Yuan, and H.H. Lin, "Mechanical properties, phases and microstructure of ultrafine hardmetals prepared by WC–6.29Co nanocrystalline composite powder," *Mater. Sci. Eng. A,* **392** [1–2] 335–339 (2005).

[95] C. Wang, L. Cheng, and Z. Zhao, "FEM analysis of the temperature and stress distribution in spark plasma sintering: Modelling and experimental validation," *Comput. Mater. Sci.,* **49** [2] 351–362 (2010).

[96] C.Y. Ho and T.K. Chu, *Electrical Resistivity and Thermal Conductivity of Nine Selected AISI Stainless Steels*. Purdue University, Center for Information and Numerical Data Analysis and Synthesis (CINDAS), 1977.

[97] J.W. Zimmermann, G.E. Hilmas, W.G. Fahrenholtz, R.B. Dinwiddie, W.D. Porter, and H. Wang, "Thermophysical Properties of ZrB_2 and ZrB_2 –SiC Ceramics," *J. Am. Ceram. Soc.,* **91** [5] 1405–1411 (2008).

[98] H.K. Bowen, “Basic research needs on high temperature ceramics for energy applications,” *Mater. Sci. Eng.*, **44** [1] 1–56 (1980).

[99] R.G. Pigeon and A. Varma, “Quantitative phase analysis of Si3N4 by X-ray diffraction,” *J. Mater. Sci. Lett.*, **11** [20] 1370–1372 (1992).

[100] D. Giuntini, J. Raethel, M. Herrmann, A. Michaelis, and E.A. Olevsky, “Advancement of Tooling for Spark Plasma Sintering,” *J. Am. Ceram. Soc.*, n/a–n/a (2015).